Applied Catalysis O: Open 199 (2025) 207027

Contents lists available at ScienceDirect

Applied Catalysis O: Open

journal homepage: www.elsevier.com/locate/apcato

Efficient organic pollutant mineralization via PMS-sonophotocatalysis with doped-ZnO-CNT aerogels

Queralt Bautista [a], Majdi Benamara [b,**], Shanyu Zhao [b], Elvira Gómez [a,c], Albert Serrà [a,c,*]

[a] Grup d'Electrodeposició de Capes Primes i Nanoestructures (GE-CPN), Departament de Ciència de Materials i Química Física, Universitat de Barcelona, Martí i Franquès, 1, E-08028 Barcelona, Catalonia, Spain
[b] Laboratory for Building Energy Materials and Components, Swiss Federal Laboratories for Materials Science and Technology (Empa), Überlandstrasse 129, 8600 Dübendorf, Switzerland
[c] Institute of Nanoscience and Nanotechnology (IN^{2}UB), Universitat de Barcelona, E-08028 Barcelona, Catalonia, Spain

ARTICLE INFO

Keywords
Zinc oxide aerogels
Pollutant removal
Doping agents
Multi-walled carbon nanotubes
Heterogeneous catalysis

ABSTRACT

This study investigates some characteristics of multi-walled carbon nanotube (MWCNT)-integrated zinc oxide (ZnO)-based aerogels doped with aluminum (A4ZO), gallium (G5ZO), and indium (I1ZO). The objective of this study is to enhance the removal of pollutants in environmental remediation. The morphology attributes of the aerogel were found to significantly influenced by the inclusion of dopants. Differences in particle aggregation and dispersion were observed in the scanning electron microscopy (SEM) images. X-ray diffraction (XRD) revealed that the hexagonal wurtzite structure of ZnO remained throughout all the samples, and Brunauer–Emmett–Teller (BET) analysis showed that their mesoporous nature and surface areas were enlarged. Photoluminescence (PL) spectra and Fourier-transform infrared (FTIR) spectroscopy displayed how dopants changed the defect density and optical properties of ZnO. Furthermore, under the combined effect of visible light, sonication, and peroxymonosulfate (PMS) activation, the I1ZO-CNT aerogel exhibited notable efficacy in degrading tetracycline, with a degradation efficiency of 97.6 %. The enhanced efficiency of the I1ZO-CNT aerogel was attributed to three factors: effective light harvesting, high charge transfer efficiency, and robust reactive oxygen species (ROS) generation. Furthermore, the stability of the doped ZnO-CNT aerogel was demonstrated by reusability tests, which revealed minimal leaching of dopants. These findings underscore the promise of doped ZnO-CNT aerogels in sustainable wastewater treatment applications.

1. Introduction

Apart form the agriculture, the chemical and pharmaceutical industries generate toxic and non-degradable organic compounds, thus producing wastewater. Even in low concentrations, these pollutants pose a serious danger for aquatic ecosystems and human health [1–5]. However, conventional wastewater treatment methods like adsorption and filtration generally have limited capacity for the complete removal of these contaminants, leading to residual pollution. This limitation emphasizes the vital need for innovative, cost-effective, and versatile methods to guarantee clean and safe water supplies [1,5–8]. In this regard, advanced oxidation processes (AOPs) represent a valuable treatment technology that utilizes highly reactive radicals, including hydroxyl radicals (•OH), to mineralize pollutants into simple, non-toxic molecules [2,9–16].

Among these AOPs, the activation of peroxymonosulfate (PMS) to produce sulfate radicals ($SO_4^{\bullet -}$) has attracted much attention owing to its high efficiency and environmental friendliness. PMS activation strategies range from heating and transition metals to microwaves and sonication. Sonolysis, for instance, utilizes the mechanism of acoustic cavitation, a process where microbubbles are created and expanded, before collapsing to produce hydroxyl radicals that indeed degrade pollutants [1,4,17–21]. Photolysis and photocatalysis, on the other hand, uses light radiation to produce •OH and superoxide ($O_2^{\bullet -}$) radicals from water and oxygen, respectively. Synergistic effects on degradation and mineralization efficiencies have been demonstrated for

* Corresponding author at: Grup d'Electrodeposició de Capes Primes i Nanoestructures (GE-CPN), Departament de Ciència de Materials i Química Física, Universitat de Barcelona, Martí i Franquès, 1, E-08028 Barcelona, Catalonia, Spain.
** Corresponding author.
E-mail addresses: majdibenamara1@gmail.com (M. Benamara), a.serra@ub.edu (A. Serrà).

https://doi.org/10.1016/j.apcato.2025.207027
Received 12 November 2024; Received in revised form 26 December 2024; Accepted 6 January 2025
Available online 8 January 2025

combined multiple AOPs (e.g., the combination of PMS activation with sonolysis or photolysis). Yet high energy requirements and non-complete mineralization remain as challenges to improve [17,22–24].

Materials science is crucial in pushing these limits further. Aerogels are lightweight highly porous materials with extreme surface areas and are synthesized via sol-gel methods and followed by supercritical drying [25–28]. Such unique properties make aerogels ideal for use in catalysis, water treatment, and environmental remediation The incorporation of carbon-based materials, such as multi-walled carbon nanotubes (MWCNTs), into aerogels serves to enhance their functionality [26,27,29–31]. MWCNTs present advantageous properties, such as excellent adsorption capacities, high conductivity, as well as the ability to accommodate various catalytic materials, including metals and semiconductors. It is this synergy that has positioned aerogels as effective platforms for advanced oxidation reactions, making them highly appropriate for the degradation of pollutants [32–36]. Moreover, some photocatalysts like zinc oxide (ZnO) remain very promising based on several adjectives such as versatile morphologies, high surface-to-volume ratio non-toxicity, and ease of synthesis. However, the relatively wide bandgap of ZnO (~3.2 eV) restricts its photocatalytic activity to the ultraviolet spectrum [37–42]. Various research possibilities observed that doping ZnO with calcium, gallium, or indium improves its photocatalytic properties, morphological stability, and light responsiveness in the visible range making it applicable for advanced environmental purposes [37,43–45]. It is important to mention that the incorporation of lattice defects by calcium, an alkaline earth metal, leads to a slight bandgap narrowing, enhancing visible-light harvesting and at the same time the surface activity and structural stability. The narrowing of the bandgap by gallium, a group III element, enables the better utilization of visible light and the reduction of electron-hole recombination through the implementation of controlled defect engineering. Moreover, its ionic radius resembles that of Zn^{2+}, causing little to no lattice strain. In addition, the much larger ionic radius of indium induces considerable lattice distortions and defects, which in turn boost light absorption, charge carrier mobility and ultimately photocatalytic activity. These dopants serve to adjust the electronic and structural characteristics of ZnO, altering the bandgap and allowing for extended light absorption leading to increased reactive species production and tailoring for specific purposes in the treatment of environmental pollutants [18,43,46,47].

Herein, we report the design and assessment of multifunctional aerogels made of ZnO doped with calcium, gallium, or indium, incorporated with MWCNT for the improvement of photocatalytic performance. This research exploits the high surface area of the aerogel, as well as the synergistic effects of ultrasonic agitation in combination with visible light irradiation to activate PMS and thus facilitate the degradation of organic pollutants in single- and multi-component solutions. This innovative approach demonstrates the potential of doped ZnO-based aerogels in advancing cost-effective and sustainable methodologies for water treatment, thereby addressing critical challenges in environmental remediation.

2. Experimental section

2.1. Synthesis and characterization of ZnO-based aerogels

2.1.1. Synthesis of doped ZnO nanoparticles

Al-doped ZnO, In-doped ZnO, and Ga-doped ZnO nanopowders were synthesized using the sol–gel method. To prepare these nanopowders, three separate solutions were made. For each solution, 16 g of zinc acetate dihydrate ($Zn(CH_3COO)_2{\cdot}2H_2O$; ≥99.0 %, Sigma-Aldrich) was dissolved in 112 mL of methanol (99.8 %, Sigma-Aldrich), which served as the solvent. The mixtures were stirred at room temperature for 10 min to ensure complete dissolution. After this initial stirring, an appropriate amount of dopant precursor was added to each solution. For the first solution, aluminum nitrate nonahydrate ($Al(NO_3)_3{\cdot}9H_2O$; ≥98 %, Sigma-Aldrich) was added as the dopant precursor to achieve an Al:Zn atomic ratio of 4 %. In the second and third solutions, gallium nitrate hydrate ($Ga(NO_3)_3{\cdot}H_2O$) and indium chloride ($InCl_3$) were added as dopant precursors to achieve Ga:Zn and In:Zn atomic ratios of 5 % and 1 %, respectively. The solutions were then stirred for an additional 15 min to ensure homogeneity. The resulting mixtures were transferred to an autoclave for drying under supercritical conditions using ethanol. This step was followed by calcination of the synthesized powders in an air muffle furnace at 400 °C for 2 h to achieve the desired crystal structure and composition. The synthesized nanopowders were designated as A4ZO, G5ZO, and I1ZO, corresponding to Al4%-doped ZnO, Ga5%-doped ZnO, and In1%-doped ZnO nanoparticles (NPs), respectively. The selected dopant compositions of aluminum (4 at. %), gallium (5 at. %), or indium (1 at. %) were informed by prior research on doped ZnO systems and tailored for this study with the objective of achieving an optimal balance between photocatalytic performance and material stability. Aluminum doping at 4 % is known to enhance structural stability and UV emission [48], while gallium doping at 5 % introduces moderate lattice distortions that improve visible light absorption [47]. Indium doping at 1 % was selected for its significant ability to create oxygen vacancies and enhance defect density, which are critical for reactive oxygen species (ROS) generation and PMS activation [18]. These concentrations were selected to optimize the catalytic efficiency of the ZnO aerogels while maintaining their structural integrity.

2.1.2. Synthesis of doped ZnO-based CNT aerogels

In instances where the sodium alginate gel exhibits instability in aqueous environments, a control alginate-NP composite aerogel was prepared for comparison. The control sample was subjected to an aqueous pollutant solution to ascertain its stability. However, the instability of the alginate precluded the acquisition of data. To enhance the mechanical stability of the aerogels, multi-walled carbon nanotubes (MWCNTs) were incorporated into the structure. The incorporation of MWCNTs into the aerogel matrix and coating with nanoparticles enhances stability, enabling the aerogels to withstand sonophotocatalysis tests in water under visible light illumination [49].

To prepare the doped ZnO/CNT aerogels, the process begins with the creation of two separate solutions. The first solution is a mixture of MWCNT and doped zinc oxide nanoparticles (A4ZO, G5ZO, and I1ZO). Specifically, 50 mg of MWCNT and 200 mg of doped ZnO NPs are added to 10 mL of deionized (DI) water. This mixture is then subjected to magnetic stirring at room temperature until a homogeneous black solution is achieved. This step ensures that the carbon nanotubes and nanoparticles are uniformly dispersed in the water, forming a stable suspension. Simultaneously, a second solution is prepared using sodium alginate, a natural polysaccharide. In this step, 0.2 g of sodium alginate is dissolved in 10 mL of DI water. The mixture is then stirred magnetically at an elevated temperature of 65 °C until it becomes viscous and transparent. Once both solutions are ready, they are combined while maintaining a temperature of 65 °C. The combined mixture is stirred magnetically until a viscous solution is observed. The blending of the two solutions at an elevated temperature ensures that the MWCNT and doped ZnO are evenly distributed within the sodium alginate matrix, forming a uniform precursor solution for the aerogel. The next step involves shaping the precursor into beads by dropping the viscous solution into a 2 wt% calcium chloride ($CaCl_2$) solution. This mixture is left to react overnight. The calcium ions in the $CaCl_2$ solution cross-link with the sodium alginate, forming a solid hydrogel structure around the nanoparticles and MWCNT. This cross-linking process is crucial as it stabilizes the structure and provides mechanical strength to the aerogel. Following the gelation, the formed beads are thoroughly washed several times with ethanol to remove any unreacted materials and impurities. The cleaned and ethanol-exchanged gel beads are then subjected to supercritical drying using CO_2. This drying technique removes the ethanol without collapsing the delicate gel structure, resulting in the final doped ZnO/CNT aerogel samples. The end product is a lightweight,

porous aerogel that incorporates the beneficial properties of both doped ZnO nanoparticles and carbon nanotubes for photodegradation of organic pollutant. More details about the preparation method are shown in Fig. S1. This material has potential applications in areas such as catalysis, sensing, or environmental remediation, thanks to its unique combination of high surface area, conductivity, and catalytic activity. The prepared aerogels samples are called A4ZO-CNT, G5ZO-CNT, and I1ZO-CNT basing on the zinc oxide nanoparticles doped by Al 4 at. %, Ga 5 at. %, and In 1 at. % with MWCNT, respectively.

2.1.3. Characterizations of the prepared nanoparticles and aerogels

The physicochemical properties of the synthesized materials were investigated using a variety of techniques, including: determining crystalline structure, morphology, chemical composition and optical properties. Concentrations of aluminum, gallium, and indium dopants in ZnO were measured by inductively coupled plasma mass spectrometry (ICP-MS) with PerkinElmer NexIon 2000 instrument. Underneath, the samples were dissolved in a 3:1 mix of nitric acid (65 %) and hydrochloric acid (37 %). X-ray diffraction (XRD) was used to determine the crystalline structure of both the doped ZnO nanopowders and the doped ZnO-CNT aerogels, with measurements taken within the 2θ range of 20° to 70° using a Bruker Philips X-Pert diffractometer equipped with Ni β-filtered Cu-Kα radiation (1.54178 Å). The morphology and phase constitution of the synthesized nanopowders were examined using scanning electron microscopy (SEM) with a Zeiss GeminiSEM 460, which provided detailed high-resolution images. The specific surface area of the materials was measured using the Brunauer–Emmett–Teller (BET) method, derived from N_2 adsorption-desorption isotherms at 77 K, utilizing a Micromeritics 3Flex Surface Characterization Analyzer. Density measurements, including true, absolute, skeletal, and apparent volumes, were obtained using an AccuPyc 1340 Pycnometer, which uses an inert gas displacement method. Optical properties were analyzed through UV–visible spectroscopy with a Shimadzu UV-3101PC spectrophotometer, covering a wavelength range from 200 to 800 nm. Photoluminescence (PL) spectra were recorded using a NanoLog Horiba modular spectrofluorometer, which employed a Xenon lamp with an excitation wavelength of 325 nm; the emission spectra were measured between 350 and 800 nm at room temperature. Fourier-transform infrared spectroscopy (FTIR) was conducted using a Bruker Vector 22 to identify functional groups and confirm the presence of dopants within the materials. Thermogravimetric analysis (TGA) was performed using a Perkin Elmer TGA 8000 to assess the thermal stability and decomposition behavior of the synthesized materials (see discussion in the supporting information).

2.2. Study of PMS activation by doped-ZnO-CNT aerogels

Sulfate radicals were indirectly determined using a spectrophotometric method relying on their ability to oxidize Ce(III) to Ce(IV). A solution of 6 mM $Ce_2(SO_4)_3$ and 0.6 mM PMS at a pH of 7.0 was prepared, and the catalyst was subsequently added to the solution. The absorbance of Ce(IV) at 320 nm was measured over a 90-min period under the following conditions: dark, visible light, sonication, and a combination of visible light and sonication. UV–vis spectrophotometry was used to obtain the data. In the absence of PMS, no oxidation of Ce(III) was observed. The time-dependent formation of Ce(IV) was employed to calculate the concentration of sulfate radicals, with a calibration curve constructed from standard solutions of Ce(IV) serving as the basis for this calculation. The concentration of hydroxyl radicals was determined by monitoring the degradation of fluorescein sodium salt (Sigma-Aldrich), a fluorescence-based probe. A solution of 8 μM fluorescein sodium salt (excitation at 303 nm, emission at 515 nm) was prepared and the catalyst was immersed in 10 mL of this solution under the following conditions: in the dark, in the presence of visible light, with sonication, and with a combination of visible light and sonication, all in the presence of 0.6 mM of PMS. The experiments conducted in the absence of PMS were not evaluated, as this section is focused exclusively on the study of PMS activation. The fluorescence intensity of the solution was recorded using an AMINCO-Bowman Series 2 spectrofluorometer with a quartz microcell at 25 °C. A calibration curve was constructed by measuring the fluorescence intensity of standard solutions with known concentrations of fluorescein sodium salt, thereby enabling the calculation of hydroxyl radical concentrations.

2.3. Catalytic experiments

To analyze the catalytic performance of the three doped ZnO-CNT aerogels, a series of experiments were conducted to assess the impact of various factors—such as visible light, sonication, PMS presence, and combinations thereof—on the degradation and mineralization of organic pollutants. A 20 mg L^{-1} solution of tetracycline (TC) was prepared and adjusted to pH 7. The solution was incubated at 20 °C under dark conditions to ensure any degradation was solely due to LED illumination or ultrasounds. Before each experiment, adsorption-desorption equilibrium was established between the catalyst and the TC solution. To achieve this, 10 mL of the 20 mg L^{-1} TC solution at pH 7 were mixed with 1 mg of catalyst and stirred magnetically in the dark for 30 min.

To monitor TC degradation, UV–vis spectra changes were tracked using a UV–vis spectrophotometer (Shimadzu UV-1800). The effect of visible light was tested by exposing the catalyst-adsorbed TC solution to a 1.6 W cylinder of white LED light ($2.2{\cdot}10^{-3}$ W/cm^2) for 90 min, with periodic activation and deactivation of the LED for UV–vis readings at the maximum wavelength. To examine the influence of PMS (oxone, Merck)—composed of $KHSO_5{\cdot}0.5\ KHSO_4{\cdot}0.5\ K_2SO_4$—40 μL of a 150 mM solution were added to the catalyst-equilibrated TC solution. Measurements were taken at various intervals over a 90-min period. The effect of ultrasonication was also investigated by subjecting the catalyst-TC solution to ultrasound for 90 min, with intermittent pauses for UV–vis measurements. The temperature was controlled using a cooling system to prevent overheating during sonication, and all samples were kept in the dark.

Once the effects of photocatalysis, sonocatalysis, and PMS on TC degradation were individually evaluated, various combinations of two parameters were studied. In the sono-photocatalysis experiment, the catalyst was subjected to both sonication and LED illumination for 90 min. The LED and sonicator were stopped before taking UV–vis readings. The other two experiments investigated the performance of PMS combined with either ultrasound or visible light. For the PMS-sonocatalysis experiment, sonication was applied for 90 min with pauses for UV–vis readings. In the PMS-photocatalysis experiment, the catalyst-adsorbed TC solution was irradiated with visible light under similar on-off conditions for measurement. Finally, the combined effect of all three factors—light, ultrasound, and PMS—was assessed. In this case, the TC solution in equilibrium with the catalyst was both sonicated and illuminated for 90 min while 40 μL of PMS solution were added. UV–vis spectra were collected at intervals throughout the experiment, with the LED and sonicator turned on and off as needed.

After each experiment, total organic carbon (TOC) was measured using high-temperature combustion with a TOC-VCSH analyzer (Shimadzu) to assess mineralization. The effectiveness of PMS-sonophotocatalysis using doped ZnO-CNT aerogels was also tested on other organic pollutants. Two multi-pollutant solutions, each at pH 7, were prepared: one with TC, methylene blue (MB), levofloxacin (LEV), and rhodamine B (Rh-B) at 20 mg L^{-1}, and another at 80 mg L^{-1}. Before starting the experiments, 10 mL of each solution were added to 1 mg of catalyst and stirred in the dark to achieve adsorption-desorption equilibrium. Afterward, 40 μL of a 150 mM PMS solution were introduced, and the solutions were subjected to ultrasound and visible light irradiation. The diluted solution was tested at 30, 60, and 90 min, while the concentrated solution was tested at 60, 120, 180, 240, and 300 min. Solutions were then filtered through 0.45-μm syringe filters, and mineralization was determined via TOC loss. The initial and equilibrium

solutions were also measured for comparison. The experiments were conducted in triplicate for each of the three catalysts.

The reusability of the most effective catalyst was further evaluated to determine its applicability under all three conditions—40 μL of a 150 mM PMS solution, visible light, and ultrasound—for multi-pollutant solution of 20 mg L^{-1}. The catalyst's reusability was tested over 10 cycles of 90 min. After each cycle, mineralization was assessed by measuring the total organic carbon (TOC).

3. Results and discussion

3.1. Synthesis and characterization of ZnO-based aerogels

Prior to characterizing the aerogels, the amount of metal dopants in ZnO was measured by ICP-MS. Results showed successful incorporation of aluminum, gallium, and indium into ZnO-based nanoparticles, with concentrations of ~4 at. % for aluminum, 5 at. % for gallium, and 1 at. % for indium. These values were found to closely correlate with the targeted dopant levels, confirming the effectiveness of the doping process. The SEM images provide insight into the morphology of various nanoparticles and composite materials, with a scale bar of 200 nm for reference (Fig. 1). Fig. 1a-c illustrates the disparate morphologies of the nanoparticles A4ZO, G5ZO, and I1ZO, respectively. The A4ZO nanoparticles displayed densely packed clusters with irregular, granular shapes and rough surfaces, indicative of substantial agglomeration (Fig. 1a). The particles were generally observed to be below 200 nm in size. This morphology suggested that the aluminum doping in ZnO played a role in the formation of compact and aggregated structures. In contrast, the G5ZO nanoparticles (Fig. 1b) also exhibited a clustered morphology, albeit with slightly more defined and less densely packed structures compared to those of the A4ZO nanoparticles. The particle size remained below 200 nm. The dissimilarities in morphology indicated that gallium doping influences the nanoparticle growth process, resulting in a more uniform distribution and potentially less aggregation than in the aluminum-doped samples. In contrast, the I1ZO nanoparticles (Fig. 1c), which exhibited a more spherical and uniform morphology, accompanied by smoother surfaces and a diminished tendency to agglomerate. To estimate the average crystallite sizes of the prepared nanoparticles, we used ImageJ software to analyze the particle size distribution histograms of each nanoparticle sample presented in Figs. S2-a, S2-b, and S2-c for the A4ZO, G5ZO, and I1ZO samples, respectively. This analysis shows that the particle sizes remained below 200 nm, with average sizes of 63 nm, 53 nm, and 50 nm for the A4ZO, G5ZO, and I1ZO samples, respectively. The particles remained below 200 nm in size. This indicated that indium doping affected the surface properties and crystallinity of ZnO, resulting in a more homogeneous and less aggregated morphology compared to A4ZO and G5ZO.

Fig. 1d-e illustrate the morphology of MWCNTs. The SEM images demonstrated a fibrous and tubular structure with extensive entanglement, which is characteristic of CNT materials. The MWCNTs exhibited a relatively uniform diameter and formed an interconnected network, indicating the presence of strong van der Waals interactions that contributed to the maintenance of the fibrous network structure. This morphology proved advantageous for enhancing the mechanical and electrical properties when MWCNTs were used as a composite matrix with nanoparticles. The SEM micrographs (Fig. 1f, g, h, and i) depict the

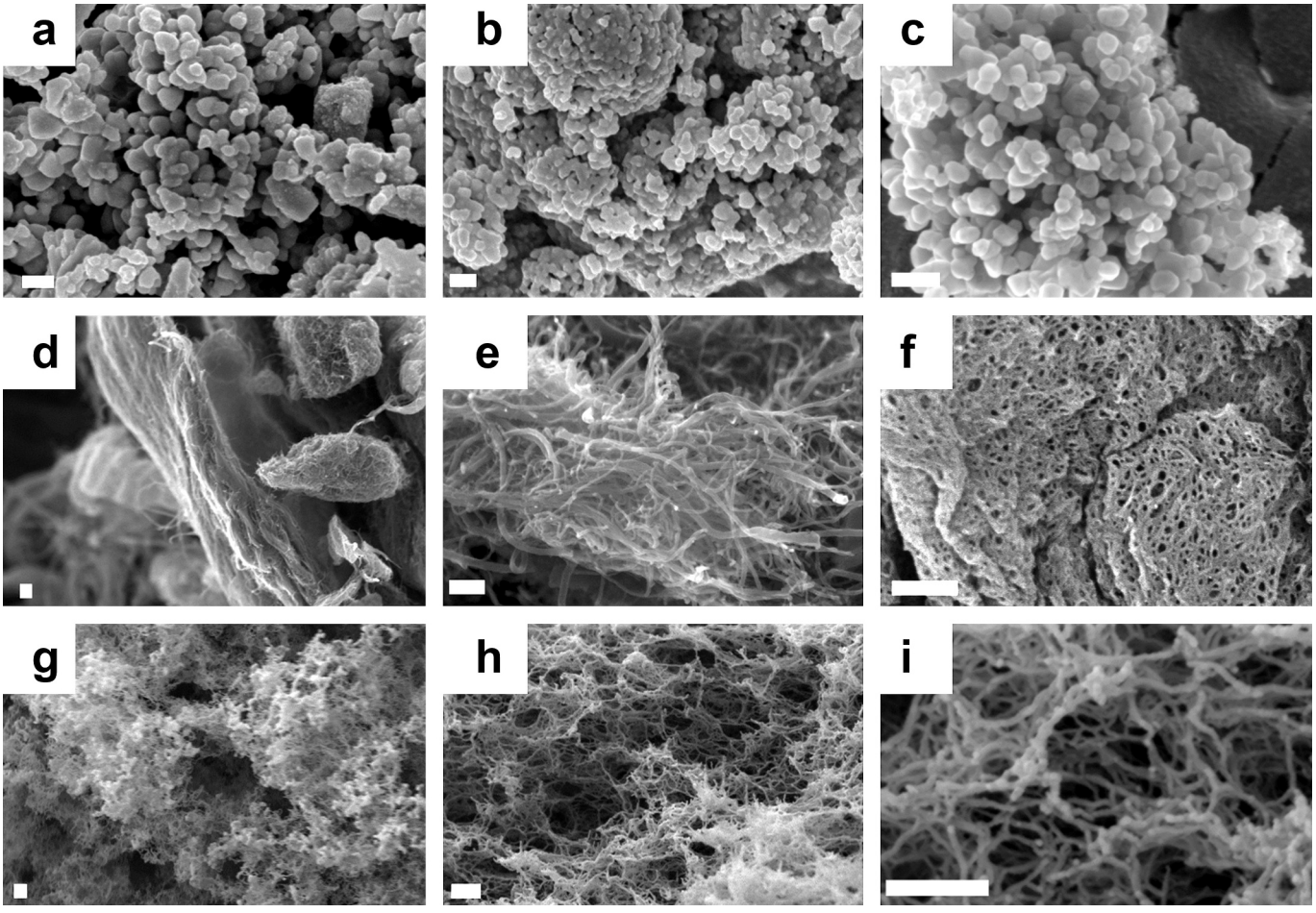

Fig. 1. FE-SEM micrographs of (a) A4ZO, (b) G5ZO, and (c) I1ZO nanoparticles; (d, e) MWCNTs; and (f) A4ZO-CNT, (g) G5ZO-CNT, and (h, i) I1ZO-CNT aerogels. The scale bar is 200 nm.

morphology of the aerogels composed of the prepared nanoparticles and MWCNTs, specifically A4ZO-CNT, G5ZO-CNT, and I1ZO-CNT, respectively. Fig. 1f depicts the A4ZO-CNT aerogel, which exhibits a porous structure with A4ZO nanoparticles embedded within the MWCNT network. The CNTs provided a supporting framework that facilitated the dispersion of the nanoparticles throughout the aerogel. Fig. 1g depicts the G5ZO-CNT aerogel, which also exhibits a porous network. However, the integration of G5ZO nanoparticles was more uniform, suggesting enhanced compatibility or interaction between the Ga-doped ZnO particles and the MWCNTs. Fig. 1h and i depict the I1ZO-CNT aerogel, which exhibited a highly porous and interconnected structure with a high surface area. The I1ZO nanoparticles were observed to be well-dispersed within the CNT framework, resulting in the formation of a cohesive network with minimal agglomeration. This indicated that the introduction of In doping had the effect of enhancing the interaction between the ZnO nanoparticles and the CNTs, which resulted in the formation of a more uniform and stable composite structure.

Fig. 2a illustrates the XRD patterns of the aerogels A4ZO-CNT, G5ZO-CNT, and I1ZO-CNT. The primary peaks were consistent with the hexagonal wurtzite structure of ZnO. This structure was retained across all samples, indicating that the incorporation of dopants (Al, Ga, and In) did not result in a significant alteration of the ZnO lattice. The aforementioned peaks, which correspond to crystallographic planes such as (100), (002), and (101), remained consistent across the aerogels, indicating

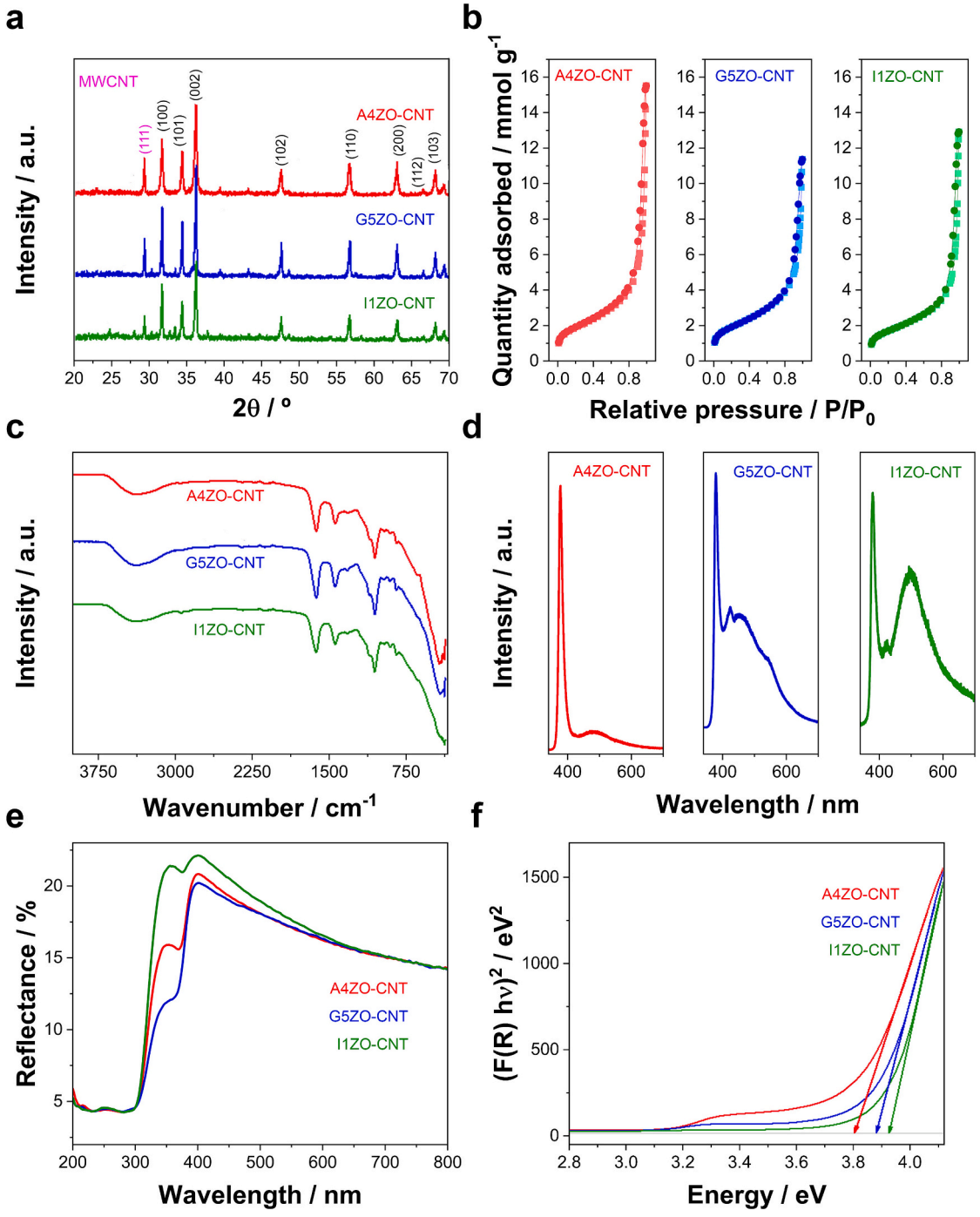

Fig. 2. (a) X-ray diffraction patterns, (b) BET surface area, (c) FTIR spectra, (d) PL spectra, (e) DRS UV–vis spectra, and (f) Tauc plots of A4ZO-CNT (red), G5ZO-CNT (blue), and I1ZO-CNT (green) aerogels. (For interpretation of the references to colour in this figure legend, the reader is referred to the web version of this article.)

that the ZnO framework was stable despite the presence of MWCNTs and doping [18]. The additional peak observed at approximately 29.5° was attributed to the MWCNTs, which typically exhibit a peak near 25.6° in their graphitic (111) plane (Fig. S3a) [50,51]. This shift to 29.5° indicated that interactions between the ZnO matrix and the MWCNTs, potentially due to mechanical strain and bonding, were influencing the nanotubes' interlayer spacing, compressing the carbon nanotubes within the structure.

A comparison of the aerogels with their powder (Fig. S3b) counterparts revealed the presence of broader peaks in the aerogel samples, which was indicative of smaller crystallite sizes and increased strain in the ZnO matrix. This broadening was attributed to the disruption of the ZnO crystallinity by the MWCNTs, which introduced strain and defects [52]. Moreover, the supercritical drying process employed to fabricate the aerogels was likely to introduce additional mechanical strain, which contributed to the disorder observed in the XRD peaks [53]. While the primary ZnO peak positions remained consistent between the aerogels and powders, the dopants' interaction with the CNTs likely contributed to the observed peak broadening and the CNT peak shift from 25.6° to 29.5°. The retention of the ZnO wurtzite structure, peak broadening, and CNT peak shift indicated the presence of robust interactions between the ZnO matrix, dopants, and MWCNTs in the aerogel samples.

The BET isotherms for the ZnO nanoparticles (Figs. S4a-c) provided insights into the surface properties of the ZnO samples doped with different elements (Al, Ga, and In, respectively). Each isotherm exhibited a characteristic Type IV curve with a discernible hysteresis loop, indicative of the existence of mesopores within the material [54]. The relatively high adsorption volumes observed at increased relative pressures (P/Po) indicate that these ZnO nanoparticles possess well-developed porous structures, which facilitate efficient gas adsorption. The BET analysis indicated that these nanoparticles, regardless of the dopant, exhibited a high surface area, rendering them effective for applications based on surface interactions [54].

Fig. S4d depicts the BET isotherm of the MWCNTs, which revealed a specific surface area of 105 $m^2 g^{-1}$. Furthermore, the isotherm displayed Type IV behavior with a pronounced hysteresis loop, which was indicative of mesoporous characteristics. The mesoporosity was likely attributable to the interstitial spaces between the individual nanotubes and the layered structure within the nanotubes. The observed surface area and pore structure indicated that MWCNTs represented an excellent platform for further enhancement through composite formation.

The BET isotherms for the composite aerogels (Fig. 2b) elucidated the surface properties of aerogels formed by combining the Al-, Ga-, and In-doped ZnO nanoparticles with MWCNTs, respectively. These isotherms indicated a notable enhancement in the adsorption capacity relative to the individual components, underscoring a synergistic interaction between the ZnO nanoparticles and MWCNTs. The presence of hysteresis loops in these isotherms provided further evidence that a complex mesoporous network was formed within the aerogels, which was likely the result of interfacial interactions between the ZnO particles and the MWCNT matrix [55]. The enhanced mesoporosity and the associated increased in surface area suggest that these composite aerogels could be particularly effective in applications requiring lightweight, high-surface-area materials, such as in gas storage, environmental remediation, and advanced catalysis [31,56].

Table 1 presents a comparison of the densities and BET surface areas of powders and aerogels, illustrating the alterations that occurred during the transformation of nanoparticles into aerogels. MWCNTs exhibited a low density of 1.9883 g cm^{-3} and a high BET surface area of 105 $m^2 g^{-1}$, which is characteristic of lightweight materials with large surface areas. These properties rendered them ideal for applications involving adsorption and catalysis. The A4ZO powder, which was presumably zinc oxide-based, exhibits a markedly higher density of 5.2020 g cm^{-3} while displaying a considerably reduced surface area of 23 $m^2 g^{-1}$. A similar pattern was observed in G5ZO, which exhibited a slightly higher density of 5.3783 g cm^{-3} and a lower surface area of 12 $m^2 g^{-1}$. I1ZO exhibited the highest density at 5.8678 g cm^{-3} and the lowest BET surface area of 2 $m^2 g^{-1}$. These findings indicated an inverse relationship between density and surface area. The transformation into aerogels resulted in a notable reduction in density while simultaneously increasing the surface area. The A4ZO-CNT aerogel exhibits a density of 2.4626 g cm^{-3}, yet its BET surface area reached 147 $m^2 g^{-1}$. Similarly, G5ZO-CNT had a density of 3.1243 g cm^{-3} and a surface area of 148 $m^2 g^{-1}$. The I1ZO-CNT aerogel exhibited the most pronounced transformation, with a notable reduction in density to 2.4139 g/cm^3 and a substantial increase in surface area to 132 $m^2 g^{-1}$ from a mere 2 $m^2 g^{-1}$ in its original powder form. The transformation from powders to aerogels significantly enhanced the surface area while reducing the density, thereby creating highly porous and lightweight materials that are ideal for applications such as filtration, adsorption, and catalysis [57,58].

Table 1
BET surface area and density values of doped ZnO nanoparticles and doped ZnO-CNT aerogels.

Samples		Density / g cm^{-3}	BET surface area / $m^2 g^{-1}$
Powders	MWCNTs	1.9883	105
	A4ZO	5.2020	23
	G5ZO	5.3783	12
	I1ZO	5.8678	2
Aerogels	A4ZO-CNT	2.4626	147
	G5ZO-CNT	3.1243	148
	I1ZO-CNT	2.4139	132

The FTIR spectra of the three samples (Fig. 2c), revealed key features related to both the ZnO structure and CNTs. A broad peak around 3376 cm^{-1}, observed in all curves, was attributed to O-H stretching vibrations, which were likely due to surface hydroxyl groups or adsorbed water [59]. This broadness suggested the presence of hydrogen bonding, which may be enhanced by surface defects in ZnO and interactions with oxygen-containing groups on the CNTs, thereby contributing to the composite's hydrophilicity [60]. Further structural insight was provided by high-intensity peaks at 1161, 1421, 1020, and 401 cm^{-1}. The 1161 cm^{-1} peak was associated with C-O stretching, indicating the presence of oxygenated functional groups on the CNTs, which facilitate interaction with metal oxides [61]. The peak at 1421 cm^{-1} was attributed to C-C or C=C stretching in the sp^2 hybridized CNTs, and it also served to reflect interactions with doped ZnO. The 1020 cm^{-1} peak was indicative of Zn-O stretching in the ZnO structure, thereby suggesting the presence of a well-formed crystalline phase. Furthermore, the 401 cm^{-1} peak served to confirm the retention of the ZnO wurtzite structure. Additionally, smaller peaks at 1295, 1085, 942, 891, and 821 cm^{-1} were indicative of functional groups on the CNTs or ZnO-CNT interactions. The peak at 1295 cm^{-1} may be attributed to C-H bending, while the 1085 cm^{-1} peak could signify Zn–OH vibrations. These peaks served to highlight the structural changes or defects introduced by doping and the ZnO-CNT interaction [62–65].

The doping of ZnO with Al, Ga, or In resulted in the introduction of defects and charge carriers within the lattice, as evidenced by the observed shifts in the positions of ZnO-related peaks. The dopants, with differing ionic radii relative to Zn(II), distorted the lattice and altered the vibrational frequencies of Zn-O bonds, thereby affecting the overall material properties and interactions with CNTs [66,67]. The high conductivity and surface area of CNTs complemented the properties of ZnO. The functionalization, as evidenced by the presence of C-O and C=C peaks, facilitated the integration of the aerogel with ZnO and enhances the dispersion of ZnO within the composite. This strong interaction was corroborated by the overlapping peaks observed in the FTIR spectra, which served to highlight the synergy present within the composite structure. In conclusion, the FTIR spectra of these doped ZnO-CNT aerogels demonstrated a complex interaction between ZnO and CNTs. The broad O-H peak at 3376 cm^{-1} and distinct peaks at 1161, 1421, 1020, and 401 cm^{-1} served to confirm the successful integration. The differences in peak positions and intensities reflected the influence of

doping on the ZnO structure and its interaction with CNTs [68].

The PL spectra of ZnO-CNT aerogels (Fig. 2d) yielded valuable insights into their optical properties. The A4ZO-CNT spectrum exhibited a pronounced UV emission peak at approximately 380 nm, indicative of effective near-band-edge (NBE) emission, which was predominantly associated with excitonic recombination [69]. The aluminum doping, which is characterized by the substitution of Al^{3+} for Zn^{2+}, did not result in a notable increase in defect levels, thereby maintaining the structural integrity of the ZnO structure. The weak visible emission observed in this spectrum indicated that aluminum introduced fewer defects compared to other dopants. This allowed for more efficient radiative recombination in the UV region while minimizing defect-related emissions, such as those arising from oxygen vacancies or zinc interstitials [70]. The incorporation of MWCNTs played a pivotal role in enhancing the aerogel's overall performance, functioning as a charge transport network. The presence of MWCNTs facilitated the separation of photogenerated electron-hole pairs, thereby reducing non-radiative recombination at defect sites. This enhancement was particularly beneficial for A4ZO-CNT, where the CNTs helped to amplify the UV emission and suppress visible emissions. However, an examination of the G5ZO-CNT aerogel revealed the presence of a broader UV emission peak and a markedly stronger visible emission in comparison to the Al-doped sample. This indicated that the introduction of gallium doping resulted in the formation of additional structural defects, which subsequently led to an increase in defect-related luminescence, commonly referred to as "green luminescence." The elevated defect density, particularly that of oxygen vacancies, contributed to an increase in non-radiative recombination pathways, which diminished the intensity of UV emission despite the presence of MWCNTs that were intended to enhance charge separation [71,72].

The PL spectrum of the I1ZO-CNT aerogel exhibited a markedly intense visible emission and a diminished UV emission, suggesting that indium doping introduced the highest defect concentration among the three dopants. The larger size of In^{3+} compared to Zn^{2+} resulted in substantial distortion of the ZnO lattice, leading to the proliferation of structural defects, including oxygen vacancies [46]. The intense visible emission, typically observed in the range of 500–600 nm, indicated that defect states were the dominant factor in the recombination processes, effectively suppressing excitonic recombination and thereby reducing UV luminescence. While MWCNTs continued to facilitate electron transport and mitigate recombination at defects, the considerable number of defects introduced by indium doping resulted in pronounced defect-related emissions, which eclipsed the contributions of CNTs to UV emission enhancement. The incorporation of MWCNTs across all doped ZnO aerogels resulted in a notable enhancement in charge separation and electron mobility, which was crucial for effective performance in applications such as photocatalysis [39]. In the case of aluminum-doped ZnO, the CNTs amplified UV emission by minimizing defect-related recombination. In contrast, in gallium- and indium-doped samples, the increased number of defect states leads to stronger visible emissions that overshadow the benefits of improved charge transport. This comparison demonstrated that while MWCNTs enhanced overall performance, the specific choice of dopant was crucial in determining the PL behavior by controlling the defect density and nature in the ZnO lattice.

The diffuse reflectance spectra (DRS) and band gap characteristics of ZnO-CNT aerogels (Fig. 2e and f) demonstrate the impact of diverse dopants and the incorporation of MWCNTs on the optoelectronic properties of the materials. In the reflectance spectra, the I1ZO-CNT aerogel showed the highest reflectance in the visible range, suggesting a lower defect density. This phenomenon could be attributed to the larger ionic radius of indium, which results in a moderate distortion of the lattice and a reduction in the number of defects, including oxygen vacancies and zinc interstitials. In contrast, the reflectance of the G5ZO-CNT and A4ZO-CNT aerogels exhibited a progressive decrease, with the lowest values observed in the Al-doped samples. This pattern suggested that both gallium and aluminum introduced greater structural defects, which acted as scattering and absorption centers, thereby reducing reflectance by absorbing more light. Furthermore, the incorporation of MWCNTs enhanced charge transport by reducing electron-hole recombination at defect sites, thereby improving light absorption, particularly in the UV range. MWCNTs typically exhibit a small or negligible bandgap, with metallic MWCNTs having a bandgap close to 0 eV, while semiconducting MWCNTs have a bandgap that generally ranges from approximately less than 1 eV [73]. The presence of MWCNTs facilitates efficient electron transfer and helps to separate charge carriers, thus reducing recombination. This synergy between MWCNTs and doped ZnO enhances the photocatalytic performance, by broadening the absorption spectrum and promoting better charge carrier dynamics [74,75].

The band gap energies of the ZnO-CNT aerogels were calculated using the Kubelka-Munk function and Tauc's plot (Fig. 2f), yielding values of 3.81 eV for A4ZO-CNT, 3.88 eV for G5ZO-CNT, and 3.92 eV for I1ZO-CNT. The smallest band gap was observed in the aluminum-doped samples, which exhibited minimal distortion and fewer defect states. This can be attributed to the similarity in size between the Al^{3+} ions and Zn^{2+}, which allowed for smooth integration into the ZnO lattice. The slight increase in the band gap compared to that of pure ZnO (~3.3–3.4 eV) may be attributed to interactions between ZnO and MWCNTs, which modify the electronic states in the vicinity of the conduction band edge [76]. The application of gallium doping results in the formation of a slightly larger band gap, which can be attributed to the smaller size of Ga^{3+} ions in comparison to Zn^{2+}. This leads to a moderate distortion of the lattice, which in turn elevates the conduction band and widens the band gap. Furthermore, this phenomenon introduces additional defect states that absorb light, contributing to a reduction in reflectance within the visible range. The largest band gap (3.92 eV) is observed in indium-doped samples, which exhibit significant lattice strain induced by the larger In^{3+} ions. This results in the creation of additional defect states that impede UV emission and enhance absorption in the visible range. Across all samples, MWCNTs enhance charge mobility by reducing recombination at defect sites, particularly in the UV range. Although they did not directly alter the band gap, MWCNTs improved overall optical performance by minimizing non-radiative losses associated with defects. Ultimately, the choice of dopant was the primary factor influencing the band gap and defect density, while MWCNTs mainly enhanced charge transport and optical absorption efficiency [77,78].

3.2. Study of PMS activation by doped-ZnO-CNT aerogels

Although the heterogeneously induced mineralization of organic pollutants is influenced by various factors, such as pollutant adsorption, light penetration, catalyst hydrophilicity, agglomeration, and catalyst dosage, the role of PMS activation by doped-ZnO-CNT aerogels remains a critical focus. To hypothesize the mechanisms of PMS activation and understand how the dopant type affects catalytic sites, the activation process was evaluated under visible light, sonication, and combined treatment conditions.

Fig. 3a illustrates the discernible trends in sulfate radical production, as indicated by the absorbance at 320 nm (the maximum absorption wavelength of Ce(IV)) over the course of a 90-min reaction period [17]. The generation of Ce(IV) increased progressively under visible light irradiation for all three aerogels, indicating that photochemical activation of PMS occurred. Among the three catalysts, G5ZO-CNT exhibited the highest Ce(IV) concentration of approximately 0.20 mM after 90 min, while I1ZO-CNT demonstrated a concentration of approximately 0.19 mM, closely following the former. In comparison, A4ZO-CNT exhibited the lowest efficiency, with a Ce(IV) concentration of approximately 0.15 mM. These findings indicate that G5ZO-CNT and I1ZO-CNT demonstrated superior photocatalytic activity under visible light, potentially due to enhanced light absorption and more efficient electron transfer properties compared to A4ZO-CNT. In the absence of visible light, sonication alone was found to be an ineffective method for

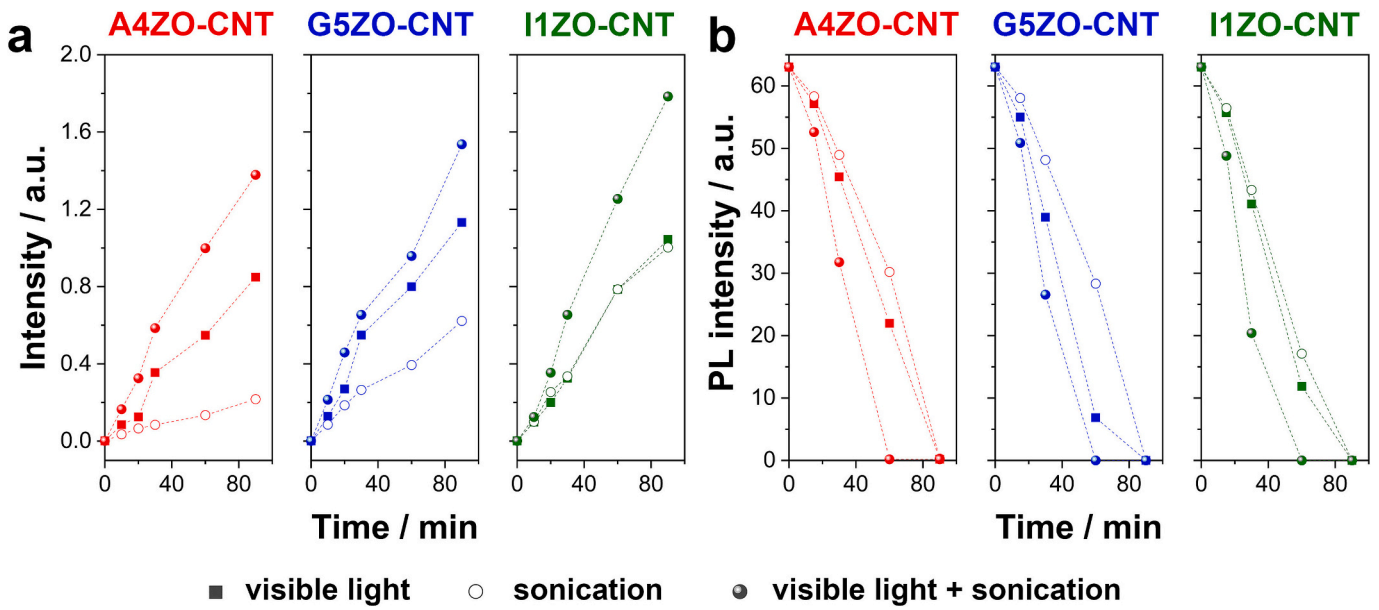

Fig. 3. (a) Time-dependent evolution of absorbance at 320 nm, corresponding to the maximum absorption wavelength of Ce(IV), and (b) time-dependent photoluminescence intensity at 515 nm (λex = 303 nm) of an 8 μM fluorescein aqueous solution. The data compare the performance of A4ZO-CNT, G5ZO-CNT, and I1ZO-CNT aerogels under three conditions: visible light, sonication, and combined visible light and sonication. Experimental conditions: [TC] = 0 mg L^{-1}, [PMS] = 0.6 mM, temperature = 25 °C, catalyst dosage = 0.1 mg mL^{-1}. All experiments were conducted in triplicate.

activating PMS, resulting in significantly lower Ce(IV) concentrations across all aerogels. The final Ce(IV) concentrations were approximately 0.04 mM, 0.11 mM, and 0.18 mM for A4ZO-CNT, G5ZO-CNT, and I1ZO-CNT, respectively. Although sonication facilitates cavitation, which improves mass transfer and generates local energy hotspots, its efficacy in sulfate radical generation remained constrained when employed as the sole activation method. Nevertheless, the disparities in performance among the aerogels continued to demonstrate that I1ZO-CNT exhibits augmented catalytic attributes, thereby facilitating superior PMS activation under the influence of cavitation effects. The combination of visible light and sonication resulted in a significant increase in Ce(IV) concentration for all aerogels, demonstrating the synergistic effect of photochemical activation and cavitation processes. The highest concentration of Ce(IV) was observed for I1ZO-CNT, at approximately 0.32 mM, followed by G5ZO-CNT, at approximately 0.28 mM, and A4ZO-CNT, at approximately 0.25 mM. These findings substantiated the hypothesis that sonication enhanced the overall efficiency of visible light activation. This was evidenced by improvements in mass transfer, acceleration of PMS decomposition, and reduction in sulfate radical loss. The combination of sonication and visible light irradiation demonstrated a particularly notable synergistic effect for I1ZO-CNT, which consistently exhibited superior performance compared to the other aerogels.

On the other hand, the temporal progression of the PL intensity of fluorescein at 515 nm (λex = 303 nm) (Fig. 3b) was used to investigate the generation of •OH radicals. The zero-order kinetics and equimolar reaction stoichiometry between •OH and fluorescein were assumed [17]. The kinetic constants revealed the enhanced performance of the catalysts under different conditions, with the combination of visible light and sonication showing the highest reaction rates. I1ZO-CNT demonstrated the highest efficiency under these conditions, exhibiting a kinetic constant of approximately 0.38 μM min^{-1}, followed by G5ZO-CNT of approximately 0.33 μM min^{-1} and A4ZO-CNT of approximately 0.28 μM min^{-1}. In the absence of sonication, G5ZO-CNT demonstrated superior performance with a kinetic constant of approximately 0.22 μM min^{-1}, followed by I1ZO of approximately 0.20 μM min^{-1} and A4ZO-CNT of approximately 0.16 μM min^{-1}. Conversely, under sonication conditions, I1ZO exhibited a higher catalytic activity with a rate constant of approximately 0.18 μM min^{-1}, closely followed by G5ZO-CNT (0.14 μM min^{-1}) and A4ZO-CNT (0.13 μM min^{-1}). These values underscored I1ZO-CNT's marked catalytic prowess, particularly in the context of combining visible light and sonication. This finding suggested that I1ZO-CNT exhibits enhanced responsiveness to dual-energy inputs in comparison to the other catalysts.

The findings unequivocally substantiate a synergistic effect between visible light and sonication in amplifying the generation of sulfate and hydroxyl radicals for all three catalysts. This combination significantly accelerates reaction kinetics in comparison to the use of visible light or sonication alone. This enhancement can be attributed to the simultaneous activation of the catalyst by photonic and mechanical energy inputs, which promote charge separation, increase the availability of reactive sites, and facilitate radical generation. The performance ranking of the catalysts, I1ZO-CNT > G5ZO-CNT > A4ZO-CNT, indicates that I1ZO-CNT is optimally tuned for the generation of sulfate and hydroxyl radicals under all tested conditions. This enhanced activity can be attributed to the advantageous structural and electronic properties of I1ZO-CNT. In contrast, G5ZO-CNT demonstrated moderate performance under visible light conditions and exhibited activity comparable to I1ZO-CNT under sonication conditions, suggesting its potential as an alternative catalyst, particularly in applications where ultrasound energy predominates. Conversely, A4ZO-CNT exhibited comparatively diminished performance across all conditions, suggesting inherent limitations in its capacity to efficiently generate or sustain reactive oxygen species. Nevertheless, A4ZO-CNT demonstrated notable enhancement in its performance when subjected to the combined effects of visible light and sonication, underscoring the pivotal role of sonication in enhancing the performance of less active materials. The enhanced activity observed in I1ZO-CNT and G5ZO-CNT is likely attributable to factors such as increased surface area, enhanced availability of active sites, and improved light absorption. These findings carry significant ramifications for the conceptualization and implementation of advanced oxidation processes. The augmented generation of radicals through the concurrent utilization of visible light and sonication offers a promising strategy for expeditious and effective degradation of organic pollutants. Among the catalysts, I1ZO-CNT exhibited the most promise for practical applications, particularly in scenarios where the synergistic effects of photonic

and ultrasound activation can be optimally realized. Further investigations into the structural and mechanistic properties of I1ZO-CNT could deepen understanding of its exceptional performance and guide the development of next-generation catalysts. In summary, the combination of visible light and sonication emerges as the most effective method for sulfate and hydroxyl radical generation, with I1ZO-CNT standing out as the most efficient catalyst. These results emphasize the importance of both catalyst properties and the synergistic effects of combined activation methods in optimizing PMS activation.

3.3. Catalytic removal of organic pollutants by synthesized ZnO-CNT aerogels

Prior to start the investigation into the catalytic removal of TC under visible light, sonication, the presence of PMS, and their combinations, the adsorption-desorption equilibrium was evaluated. To ascertain the equilibrium time and adsorption capacity, the maximum absorbance of TC at approximately 357 nm was measured over 60 min in the absence of light, sonication and PMS for each prepared aerogel. All aerogels demonstrated equilibrium after a 30-min period. The percentage of TC adsorbed by each material ranged from 3 to 12.3 %, with A4ZO-CNT exhibiting the lowest adsorption capacity at 3.6 % and I1ZO-CNT demonstrating the highest at 12.3 %.

Fig. 4a-f illustrate the degradation of TC under visible light, sonication, PMS presence, and their combinations after 90 min of treatment. Under visible light alone, the degradation efficiencies for A4ZO-CNT, G5ZO-CNT, and I1ZO-CNT were 21.2 %, 32.2 %, and 60.4 %, respectively. The I1ZO-CNT aerogel exhibited markedly enhanced activity in comparison to the other aerogels, which was likely attributable to its superior photocatalytic response. Additionally, G5ZO-CNT exhibited better performance than A4ZO-CNT, underscoring the effect of specific dopants on photocatalytic efficiency. Despite the similar BET surface areas among the aerogels, I1ZO-CNT demonstrated the highest TC adsorption. However, this difference in adsorption capacity alone did

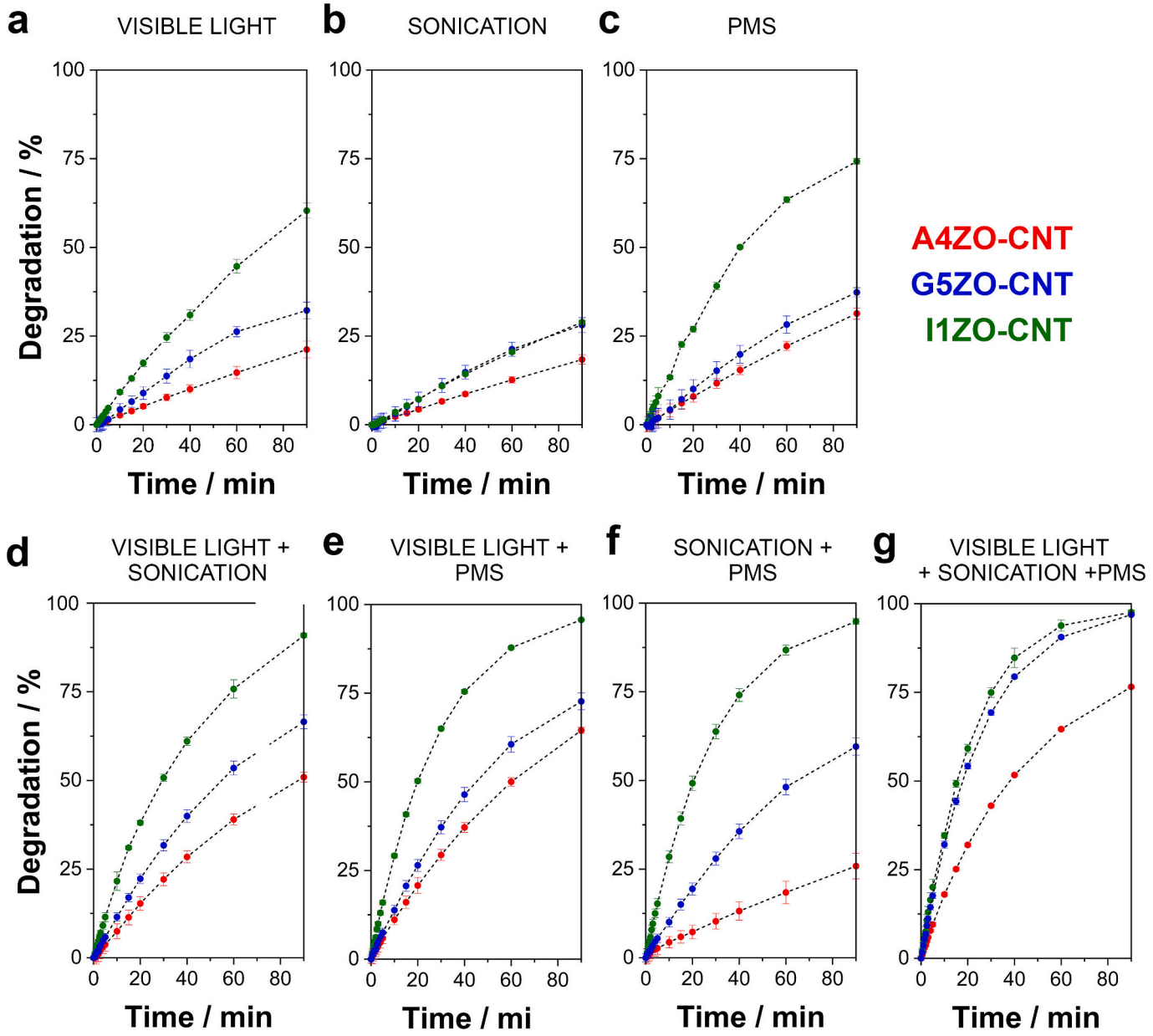

Fig. 4. Degradation performance of A4ZO-CNT, G5ZO-CNT, and I1ZO-CNT aerogels under (a) visible light, (b) sonication, (c) PMS, (d) visible light and sonication, (e) visible light and PMS, (f) sonication and PMS, and (g) visible light, sonication and PMS. Experimental conditions: [TC] = 20 mg L^{-1}, [PMS] = 0.6 mM, T = 25 °C, catalyst dosage = 0.1 mg mL^{-1}. All experiments were performed in triplicate.

not fully account for the variation in photocatalytic performance, which can also be attributed to I1ZO-CNT's enhanced light absorption and more efficient charge separation.

The degradation efficiencies observed for sonication alone were slightly lower than those achieved with visible light alone. Both G5ZO-CNT and I1ZO-CNT demonstrated comparable performance, with a degradation efficiency of 28.1 %, while A4ZO-CNT exhibited a slightly lower efficiency of 18.4 %. The impact of sonication was found to be modest, with limited enhancement of TC degradation. This limited effect indicated that sonication alone may not provide sufficient energy to generate a substantial number of reactive species. However, it did contribute to pollutant breakdown by improving mass transfer and dispersing active sites, albeit to a minor extent.

In presence of PMS – in absence of visible light and sonication – independently led to a notable enhancement in degradation across all samples, with I1ZO-CNT attaining a degradation efficiency of 74.3 %, G5ZO-CNT of 37.3 %, and A4ZO-CNT of 31.3 %. It is probable that PMS acted as a potent oxidizing agent, producing ROS that contributed to the degradation of pollutants. The results indicated that I1ZO-CNT exhibited the strongest interaction with PMS, followed by G5ZO-CNT and A4ZO-CNT. This suggests that the material composition affects the efficiency with which PMS is activated.

The combination of visible light and sonication resulted in a notable enhancement in the degradation efficiency of all aerogels. The I1ZO-CNT reached 90.9 %, the G5ZO-CNT achieved 66.6 %, and the A4ZO-CNT improved to 50.9 %. This combination was likely to have enhanced the breakdown of TC by coupling the energy input from sonication with the photocatalytic effect of visible light. This may have improved electron-hole separation and promoted the formation of ROS. The results demonstrated that I1ZO-CNT exhibited the most optimal performance, indicating that indium doping was more efficacious under these combined conditions.

The combination of visible light and PMS resulted in further enhancement of degradation, yielding efficiencies of 95.7 % for I1ZO-CNT, 72.7 % for G5ZO-CNT, and 64.5 % for A4ZO-CNT. This improvement indicated a robust synergy between light-induced photocatalysis and PMS oxidation, as visible light was likely to enhance PMS activation, resulting in elevated ROS production. The superior photocatalytic and PMS-activation properties of I1ZO-CNT in this combination were highlighted by its higher efficiency, while G5ZO-CNT demonstrated a moderate improvement and A4ZO-CNT exhibited the lowest performance.

The combination of sonication and PMS yielded lower degradation rates than those observed with visible light and PMS for all aerogels. The efficiencies were 94.9 % for I1ZO-CNT, 59.6 % for G5ZO-CNT, and 25.9 % for A4ZO-CNT. It was probable that sonication contributed to the activation of PMS to a limited extent, resulting in the production of fewer ROS compared to the activation of PMS by visible light. Nevertheless, I1ZO-CNT still demonstrated a high degradation rate, indicating that it is capable of effectively activating PMS even in the absence of light.

However, the highest degradation rates were observed when visible light, sonication, and PMS were combined. In accordance with the optimal conditions, I1ZO-CNT demonstrated a near-complete degradation rate of 97.6 %, closely followed by G5ZO-CNT at 96.9 %, and A4ZO-CNT at 76.5 %. The combination of all three factors resulted in the most efficient degradation pathway. Visible light enhances photocatalysis, PMS provides strong oxidizing power, and sonication improves mass transfer and may enhance ROS generation. The superior performance of I1ZO-CNT in this combination can be attributed to its capacity to efficiently utilize each treatment factor, with G5ZO-CNT exhibiting a similar performance. A4ZO-CNT, while still achieving a high degradation rate, demonstrated a less effective performance, likely due to the less effective interaction of aluminum with these stimuli. In conclusion, the I1ZO-CNT aerogel demonstrated the most effective degradation performance across all conditions, followed by G5ZO-CNT and A4ZO-CNT. The efficacy of each aerogel was significantly influenced by the type of dopant, with indium demonstrating the highest photocatalytic efficiency and capacity to activate PMS. The combination of visible light, sonication, and PMS resulted in the most effective TC degradation for all samples, thereby underscoring the significance of synergistic interactions between photocatalysis, oxidative treatment, and mechanical activation. These findings indicate that the dopant type is a critical factor in achieving optimal degradation performance, particularly in the context of combined treatment conditions.

Fig. 5 illustrates the mineralization performance of A4ZO-CNT, G5ZO-CNT, and I1ZO-CNT aerogels for the removal of a 20 mg L^{-1} TC solution at pH 7. Upon examination of the mineralization percentages after 90 min, it becomes evident that each aerogel responded differently to each treatment condition. This reflects the impact of both the dopants and the specific catalytic mechanisms involved. In the absence of ultraviolet radiation, the mineralization of A4ZO-CNT, G5ZO-CNT, and I1ZO-CNT was observed to be 10.7 % ± 0.1 %, 12.2 % ± 1.2 %, and 16.3 % ± 0.2 %, respectively. As with the degradation of TC, I1ZO-CNT exhibited the highest mineralization under these conditions, in accordance with the aforementioned trend. Notwithstanding the relatively low mineralization percentages achieved with visible light alone, these results underscore the impact of dopant type on mineralization efficiency in each aerogel. When sonication was employed as the sole activation method, the mineralization percentages were comparable to those observed under visible light, with values of 9.9 % ± 0.2 % for A4ZO-CNT, 13.9 % ± 0.1 % for G5ZO-CNT, and 15.1 % ± 0.2 % for I1ZO-CNT. In the presence of PMS alone, there was a notable increase in mineralization efficiency, with A4ZO-CNT achieving 23.1 % ± 0.3 %, G5ZO-CNT reaching 24.2 % ± 0.4 %, and I1ZO-CNT demonstrating the highest mineralization at 48.8 % ± 0.3 %.

The combination of visible light and sonication resulted in further improvements in mineralization. The results for A4ZO-CNT, G5ZO-CNT, and I1ZO-CNT were 28.3 % ± 0.4 %, 34.5 % ± 0.6 %, and 57.3 % ± 0.2 %, respectively. The combination of visible light and PMS resulted in markedly elevated mineralization levels across all aerogels, with the following values being observed: 32.3 % ± 0.3 % for A4ZO-CNT, 36.9 % ± 0.6 % for G5ZO-CNT, and 70.9 % ± 0.3 % for I1ZO-CNT. The incorporation of PMS under visible light resulted in a notable enhancement in mineralization efficiency, with I1ZO-CNT once again exhibiting the highest performance. The highest mineralization percentages were observed with the combination of visible light, sonication, and PMS, achieving 57.3 % ± 0.4 % for A4ZO-CNT, 83.9 % ± 0.4 % for G5ZO-CNT, and 97.6 % ± 0.6 % for I1ZO-CNT. This combination yielded a markedly synergistic effect, maximizing the mineralization of TC due to the concurrent activation pathways wherein visible light and sonication enhance radical generation while PMS furnishes a consistent supply of oxidizing agents. The near-complete mineralization observed in I1ZO-CNT is indicative of its exceptional suitability for combined treatments. This is attributed to its optimal photocatalytic properties and compatibility with PMS. Additionally, G5ZO-CNT demonstrated high mineralization efficiency in this combination, whereas A4ZO-CNT exhibited improved performance but remained lower in comparison, indicating that the dopant in A4ZO-CNT is less conducive to such synergistic effects.

A comparison of the degradation and mineralization of TC revealed that, while all aerogels demonstrated significant degradation under various treatments, mineralization was generally lower, indicating that not all degraded TC was fully mineralized into simple inorganic forms. The I1ZO-CNT aerogel exhibited the highest efficiency in both degradation and mineralization, indicating that it not only effectively breaks down TC molecule but also converts it to simpler mineralized forms such as carbon dioxide. Importantly, compared to other aerogels reported in Table S1, I1ZO-CNT offers significantly enhanced performance due to its tailored structural and electronic properties, such as improved light absorption, efficient charge separation, and superior PMS activation [79–85].

The growing prevalence of multipollutant media in environmental

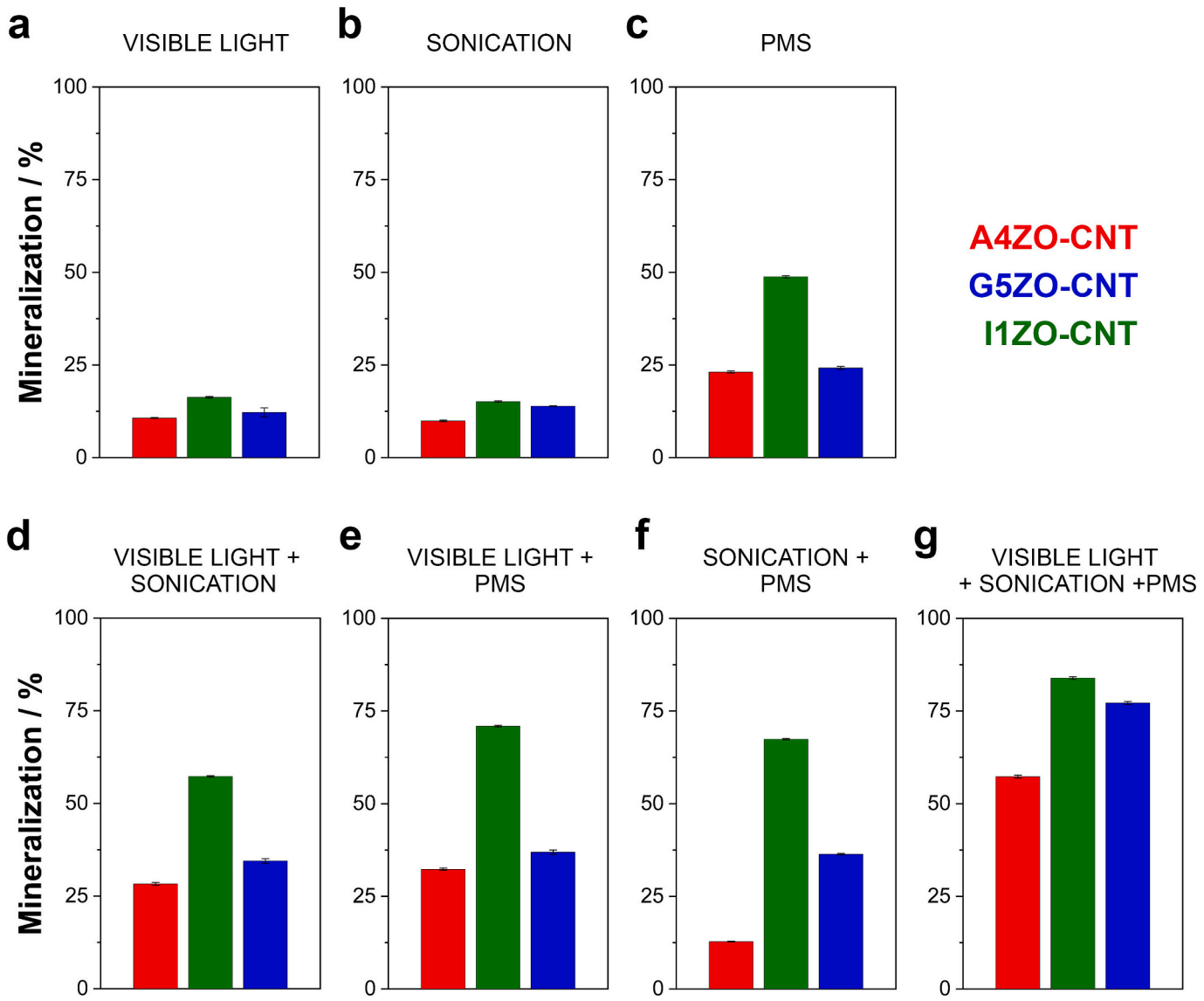

Fig. 5. Mineralization performance of A4ZO-CNT, G5ZO-CNT, and I1ZO-CNT aerogels after 90 min under various treatment conditions: (a) visible light, (b) sonication, (c) PMS, (d) visible light and sonication, (e) visible light and PMS, (f) sonication and PMS, and (g) visible light, sonication, and PMS. Experimental conditions: [TC] = 20 mg L^{-1}, [PMS] = 0.6 mM, T = 25 °C, catalyst dosage = 0.1 mg mL^{-1}. All experiments were conducted in triplicate.

contexts presents considerable obstacles to the effective treatment of wastewater. This study also examines the mineralization performance of A4ZO-CNT, G5ZO-CNT, and I1ZO-CNT in a multipollutant scenario. Two distinct pollutant solutions were evaluated: one containing 5 mg L^{-1} each of TC, LEV, LAN, and MB (total: 20 mg L^{-1}), and another containing 20 mg L^{-1} of the same pollutants (total: 80 mg L^{-1}). The mineralization efficiency of these aerogels was evaluated using a combination of visible light, sonication, and PMS activation, thereby providing insights into their performance under varying pollutant concentrations. Fig. 6a illustrates that the mineralization performance of the 20 mg L^{-1} multipollutant solution after 90 min of treatment exhibited notable discrepancies in mineralization performance among the three aerogels. The I1ZO-CNT aerogel exhibited the highest mineralization percentage, at 88.3 % ± 2.3 %, thereby demonstrating its superior efficiency in degrading and mineralizing the target compounds. Subsequently, G5ZO-CNT demonstrated a mineralization rate of 79.1 % ± 2.1 %, while A4ZO-CNT exhibited a comparatively lower efficiency of 59.8 % ± 1.9 %. These findings indicate that the lower concentration of pollutants allows for more effective interactions between the active sites of the aerogels and the reactive species generated during the treatment process, resulting in higher mineralization rates. In contrast, the mineralization performance observed for the 80 mg L^{-1} multipollutant solution over 300 min exhibited a decline in efficiency compared to the 20 mg L^{-1} scenario (Fig. 6b). The I1ZO-CNT aerogel exhibited the highest performance, with a mineralization percentage of 83.9 % ± 1.2 %. However, both A4ZO-CNT and G5ZO-CNT exhibited diminished efficiencies, with mineralization values of 56.6 % ± 2.1 % and 73.8 % ± 3.1 %, respectively. This decline can be attributed to the intensified competition among pollutants for active sites on the aerogel surfaces, which ultimately constrains the overall. These findings underscore the importance of considering the complexity of pollutant mixtures when evaluating the efficacy of photocatalytic materials. While I1ZO-CNT demonstrated superior mineralization performance overall, its effectiveness was still limited by the presence of multiple pollutants. Notwithstanding the partial mineralization observed under the prevailing conditions, it is noteworthy that PMS, due to its high oxidizing power and low chemical selectivity, can achieve near-total conversion of pollutants to inorganic forms. To illustrate, when the concentration of PMS was increased to 8 mM in both single- and multi-pollutant solutions, the mineralization efficiency for I1ZO-CNT exceeded 98 % after

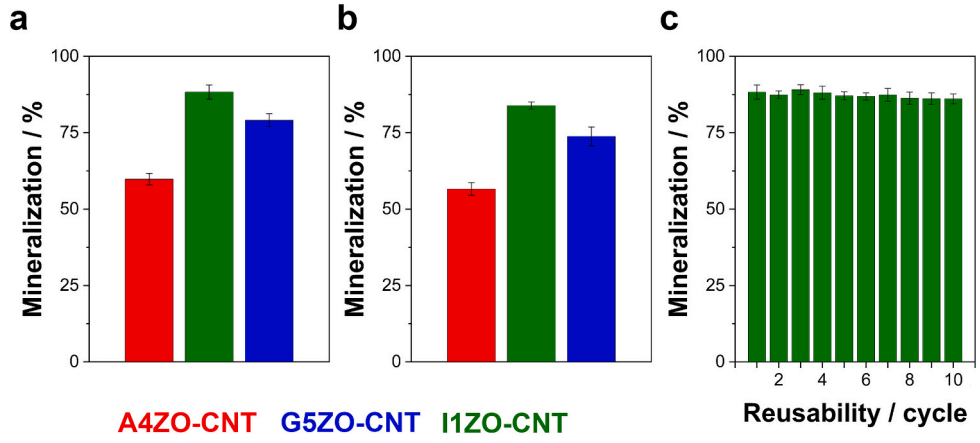

Fig. 6. Mineralization performance of A4ZO-CNT, G5ZO-CNT, and I1ZO-CNT aerogels under various conditions: (a) after 90 min using visible light, sonication, and PMS for a multipollutant solution containing TC (5 mg L^{-1}), LEV (5 mg L^{-1}), LAN (5 mg L^{-1}), and MB (5 mg L^{-1}); (b) after 300 min under the same conditions for a multipollutant solution of TC (20 mg L^{-1}), LEV (20 mg L^{-1}), LAN (20 mg L-1), and MB (20 mg L^{-1}). Experimental conditions: [pollutant] = 20 or 60 mg L^{-1}, [PMS] = 0.6 mM, T = 25 °C, catalyst dosage = 0.1 mg mL^{-1}. All experiments were performed in triplicate. (c) Reusability experiments for I1ZO-CNT aerogels conducted after 90 min under visible light, sonication, and PMS for a multipollutant solution of TC (5 mg L^{-1}), LEV (5 mg L^{-1}), LAN (5 mg L^{-1}), and MB (5 mg L^{-1}). Experimental conditions: [pollutant] = 20 mg L^{-1}, [PMS] = 0.6 mM, T = 25 °C, catalyst dosage = 0.1 mg mL^{-1}. All experiments were conducted in triplicate.

180 min. This suggests that the limitation is intrinsic to the operational parameters rather than to the inherent capabilities of the system. Accordingly, the optimization of experimental parameters, such as the concentration of PMS and the reaction time, may result in complete mineralization without the necessity of extensively investigating intermediate species within the current scope.

The results of the degradation and/or mineralization of single- and multi-pollutant solutions demonstrated that the combination of visible light, sonication, and PMS yielded near-complete degradation for I1ZO-CNT. Nevertheless, sonication seemed to exert a relatively lesser influence on its performance in comparison to the pronounced enhancement observed for G5ZO-CNT and A4ZO-CNT. The comparatively diminished impact of sonication on the performance of I1ZO-CNT, in comparison to G5ZO-CNT and A4ZO-CNT aerogels, serves to underscore the intrinsic catalytic properties of the materials. The introduction of indium doping resulted in the formation of a high density of oxygen vacancies and lattice distortions in ZnO, which served as effective catalytic sites for the activation of PMS and the generation of reactive oxygen species (ROS). These intrinsic characteristics enabled I1ZO-CNT to achieve effective pollutant degradation even in the absence of sonication, thereby reducing the relative improvement that sonication could provide. In contrast, G5ZO-CNT and A4ZO-CNT exhibited a reduced number of intrinsic defects and a slightly higher tendency for particle aggregation. For these materials, sonication played a pivotal role in surmounting these constraints by facilitating catalyst dispersion, optimizing pollutant-catalyst interactions, and enhancing the activation of PMS. Moreover, the comparatively weaker interaction between PMS and these aerogels, in comparison to I1ZO-CNT, permitted sonication to exert a more pronounced influence on ROS generation. The robust interaction between PMS and I1ZO-CNT, driven by its enhanced defect density, may have overshadowed the mechanical and mass transfer benefits provided by sonication, thereby further explaining the diminished relative impact.

This observation highlights the significance of dopant selection in optimizing the catalytic properties of aerogels. While I1ZO-CNT exhibited superior performance under all conditions due to its intrinsic catalytic efficiency, the performance of G5ZO-CNT and A4ZO-CNT could be markedly enhanced by external factors such as sonication. These findings illustrate the intricate interplay between material properties and activation methods in advanced oxidation processes, paving the way for tailored material designs for specific environmental applications.

In addition, the I1ZO-CNT aerogel exhibited remarkable reusability, as evidenced by its sustained mineralization efficiency over 10 cycles in degrading a 20 mg L^{-1} solution containing TC (5 mg L^{-1}), LEV (5 mg L^{-1}), LAN (5 mg L^{-1}), and MB (5 mg L^{-1}) (Fig. 6c). Initially, the aerogel exhibited a high mineralization efficiency of 88.3 %, with only a slight decline over the initial few cycles, indicating both stability and effectiveness. The efficiency remained above 86 % across all cycles, reflecting a robust degradation capability and suggesting that the aerogel's active sites maintained their catalytic properties well under repeated use. Although a slight decline was observed (from 88.3 % in the initial cycle to 86.1 % by the tenth), this gradual reduction is likely attributable to minor structural changes or partial deactivation of active sites, which did not significantly impact performance. The results demonstrated that the aerogel exhibited reliability and reproducibility across cycles, with minimal standard deviation. In comparison to other materials that typically exhibit a more rapid decline in efficiency due to fouling or structural degradation, the I1ZO-CNT aerogel demonstrated remarkable reusability, suggesting that it may be a more durable option for pollutant degradation, particularly when consistent, long-term performance is a priority.

Finally, the stability and durability of the catalyst were evaluated through the measurement of the release of Zn and In ions into the solution across ten reusability cycles. The results demonstrated that less than 0.3 % of the catalyst was lost as a consequence of sono-, photo-, or chemo-corrosion processes throughout the course of the experiment. The low ion release indicated that the catalyst exhibited considerable resilience to degradation processes, including ultrasonic cavitation (sonocorrosion), photodegradation under visible light exposure (photocorrosion), and chemical dissolution (chemocorrosion). Furthermore, FE-SEM was employed to examine the catalyst's surface morphology before and after the reusability cycles. The results demonstrated that no morphological or architectural alterations were observed. These findings reinforce the potential for long-term applications of the catalyst in sono-, photo-, and chemo-driven reactions.

4. Conclusions

In this study, we synthesized and characterized ZnO-based aerogels doped with aluminum (A4ZO), gallium (G5ZO), and indium (I1ZO), incorporating them with multi-walled carbon nanotubes (MWCNTs). Scanning electron microscopy (SEM) imaging demonstrated that the doping elements exerted a considerable influence on nanoparticle

aggregation, surface smoothness, and uniformity. The I1ZO sample exhibited the most spherical and least aggregated morphology, which can be attributed to the impact of indium on surface properties. X-ray diffraction (XRD) analysis demonstrated that the doped zinc oxide (ZnO) nanoparticles retained their hexagonal wurtzite structure across all aerogels. The BET analysis confirmed that the aerogels exhibited mesoporous structures with higher surface areas than their nanoparticle precursors, which is likely due to the interfacial interactions between the ZnO particles and the MWCNT matrix. Further insights into the role of each dopant in modifying ZnO's defect density and light-emission properties were provided by FTIR and PL spectra. A4ZO was observed to exhibit the most efficient UV emission, while G5ZO and I1ZO displayed intensified visible emissions linked to defect-related luminescence. The enhanced optoelectronic properties, tailored band gaps, and strong interaction between ZnO and CNTs indicate the potential of these composite aerogels in fields requiring high surface areas, effective charge transport, and specific optical behaviors.

As a final priority, the study also assessed the effective performance of ZnO-CNT aerogels for the degradation and mineralization of TC and multipollutants. The results highlighted the influence of specific material on the photocatalytic, sono-catalytic, and chemo-catalytic efficiencies under diverse activation conditions. The I1ZO-CNT aerogel demonstrated superior performance in TC degradation and mineralization compared to A4ZO-CNT and G5ZO-CNT. It achieved near-complete degradation (97.6 %) under the effect of combined visible light, sonication, and PMS treatment. This performance was attributed to the superior light absorption, efficient charge separation, and effective PMS activation of I1ZO-CNT, which collectively enhance the generation of reactive oxygen species (ROS) and catalytic activity. While G5ZO-CNT exhibited moderate catalytic efficiency, A4ZO-CNT demonstrated inferior performance, underscoring the influence of dopants on catalytic behavior under diverse activation conditions. In scenarios involving the degradation of multiple pollutants, elevated concentrations of the pollutants resulted in a reduction in the overall efficiency of mineralization due to intensified competition for active sites. Nevertheless, I1ZO-CNT exhibited the highest mineralization rates, thereby demonstrating its resilience and potential suitability for application in actual wastewater environments. Furthermore, reusability trials demonstrated the aerogel's stability, with I1ZO-CNT maintaining high mineralization efficiencies across ten cycles. The minimal leaching of Zn and In ions (less than 0.3 %) and the retention of the surface morphology after repeated use confirmed the durability of the material.

In conclusion, the I1ZO-CNT aerogel demonstrated significant promise for environmental remediation, exhibiting efficient and stable performance across diverse treatment conditions. These findings indicate that the optimization of dopant selection is essential for the maximization of degradation and mineralization efficiencies and material stability, particularly in complex pollutant matrices. This supports further research into doped aerogels for environmental applications.

CRediT authorship contribution statement

Queralt Bautista: Writing – original draft, Methodology, Investigation, Data curation. **Majdi Benamara:** Writing – original draft, Visualization, Validation, Methodology, Investigation, Formal analysis, Data curation, Conceptualization. **Shanyu Zhao:** Writing – review & editing, Visualization, Validation, Supervision, Project administration, Methodology, Investigation, Funding acquisition, Formal analysis, Data curation, Conceptualization. **Elvira Gómez:** Writing – review & editing, Writing – original draft, Visualization, Validation, Supervision, Project administration, Methodology, Investigation, Funding acquisition, Formal analysis, Data curation, Conceptualization. **Albert Serrà:** Writing – review & editing, Writing – original draft, Visualization, Validation, Supervision, Project administration, Methodology, Investigation, Funding acquisition, Formal analysis, Data curation, Conceptualization.

Declaration of competing interest

Authors declare no conflict of interest.

Data availability

Data will be made available on request.

Acknowledgements

Grant PID2020-115663GB-C32 funded by MCIN/AEI/10.13039/501100011033. Authors thank the CCiT-UB for the use of their equipment. Majdi Benamara was a Swiss Government Excellence Scholarship holder for the academic years 2023-2024 (ESKAS No. 2023.0447). Majdi Benamara expresses his gratitude to Dr. Wim Malfait, head of the Laboratory for Building Energy Materials and Components at the EMPA Research Center in Dübendorf, Switzerland, for his hospitality and support.

Appendix A. Supplementary data

Supplementary data to this article can be found online at https://doi.org/10.1016/j.apcato.2025.207027.

References

[1] E. Serrà, N. Gómez, Y. Hoda al Bast, M. Zhang, M. Duque, J. José Esplandiu, J. Esteve, B. Nogués, Sepúlveda, Wireless pulsed nanophotoelectrochemical cell for the ultrafast degradation of organic pollutants, Chem. Eng. J. 487 (2024) 150663, https://doi.org/10.1016/j.cej.2024.150663.

[2] R.J.A. Felisardo, E. Brillas, T.H. Boyer, E.B. Cavalcanti, S. Garcia-Segura, Electrochemical degradation of acetaminophen in urine matrices: unraveling complexity and implications for realistic treatment strategies, Water Res. 261 (2024) 122034, https://doi.org/10.1016/j.watres.2024.122034.

[3] X. Wang, L. Jiang, K. Li, J. Wang, D. Fang, Y. Zhang, D. Tian, Z. Zhang, D. D. Dionysiou, Fabrication of novel Z-scheme $SrTiO_3$/$MnFe_2O_4$ system with double-response activity for simultaneous microwave-induced and photocatalytic degradation of tetracycline and mechanism insight, Chem. Eng. J. 400 (2020) 125981, https://doi.org/10.1016/j.cej.2020.125981.

[4] Y. Qi Wang, K. Li, M. Yuan Shang, Y. Zhen Zhang, Y. Zhang, B. Lai Li, Y. Jiao Kan, X. Qiang Cao, J. Zhang, A novel partially carbonized Fe_3O_4@PANI-p catalyst for tetracycline degradation via peroxymonosulfate activation, Chem. Eng. J. 451 (2023) 138655, https://doi.org/10.1016/j.cej.2022.138655.

[5] D. Meroni, M. Jiménez-Salcedo, E. Falletta, B.M. Bresolin, C.F. Kait, D.C. Boffito, C. L. Bianchi, C. Pirola, Sonophotocatalytic degradation of sodium diclofenac using low power ultrasound and micro sized TiO_2, Ultrason. Sonochem. 67 (2020) 105123, https://doi.org/10.1016/j.ultsonch.2020.105123.

[6] A. Atrashkevich, S. Garcia-Segura, Engineering decentralized electrodisinfection to sustain consistent chlorine generation under varying drinking water chloride content, Appl. Catal. O Open. 195 (2024) 207012, https://doi.org/10.1016/j.apcato.2024.207012.

[7] P. Alulema-Pullupaxi, P.J. Espinoza-Montero, C. Sigcha-Pallo, R. Vargas, L. Fernández, J.M. Peralta-Hernández, J.L. Paz, Fundamentals and applications of photoelectrocatalysis as an efficient process to remove pollutants from water: a review, Chemosphere 281 (2021) 130821, https://doi.org/10.1016/j.chemosphere.2021.130821.

[8] Q. Tong, C. Li, G. Wang, Y. Wang, S. Peng, J. Wang, B. Lai, Y. Guo, Enhanced peroxymonosulfate activation by Co-bHAP catalyst for efficient degradation of sulfamethoxazole, J. Environ. Chem. Eng. 11 (2023) 109499, https://doi.org/10.1016/j.jece.2023.109499.

[9] M. Ortiz, E. Gómez, A. Serrà, Recyclable biomimetic sunflower pollen-based Photocatalyst for enhanced degradation of pharmaceuticals, Small 20 (46) (2024) 240520, https://doi.org/10.1002/smll.202405204.

[10] M. Benamara, E. Gómez, R. Dhahri, A. Serrà, Enhanced photocatalytic removal of cyanotoxins by Al-doped ZnO nanoparticles with visible-LED irradiation, Toxins (Basel) 13 (1) (2021) 66, https://doi.org/10.3390/toxins13010066.

[11] E. del Rosario Salas-Sandoval, T. Pérez-Segura, S. Garcia-Segura, A.J. dos Santos, Innovative approaches to electrochemical oxidation of bisphenol B in synthetic and complex water environments, Sci. Total Environ. 955 (2024) 176762, https://doi.org/10.1016/j.scitotenv.2024.176762.

[12] Y. Du, W. Ma, P. Liu, B. Zou, J. Ma, Magnetic $CoFe_2O_4$ nanoparticles supported on titanate nanotubes ($CoFe_2O_4$/TNTs) as a novel heterogeneous catalyst for peroxymonosulfate activation and degradation of organic pollutants, J. Hazard. Mater. 308 (2016) 58–66, https://doi.org/10.1016/j.jhazmat.2016.01.035.

[13] T. Sadeghi Rad, A. Khataee, S. Arefi-Oskoui, S. Sadeghi Rad, Y. Orooji, E. Gengec, M. Kobya, Graphene-based ZnCr layered double hydroxide nanocomposites as bactericidal agents with high sonophotocatalytic performances for degradation of

rifampicin, Chemosphere 286 (2022) 131740, https://doi.org/10.1016/j.chemosphere.2021.131740.
[14] A.N. Oliveros, J.A.I. Pimentel, M.D.G. de Luna, S. Garcia-Segura, R.R.M. Abarca, R. A. Doong, Visible-light photocatalytic diclofenac removal by tunable vanadium pentoxide/boron-doped graphitic carbon nitride composite, Chem. Eng. J. 403 (2021) 126213, https://doi.org/10.1016/j.cej.2020.126213.
[15] P. Kumar, K. Hegde, S.K. Brar, M. Cledon, A. Kermanshahi Pour, Physico-chemical treatment for the degradation of cyanotoxins with emphasis on drinking water treatment - How far have we come? J. Environ. Chem. Eng. 6 (2018) 5369–5388, https://doi.org/10.1016/j.jece.2018.08.032.
[16] M. Tayyab, S. Mansoor, Z. Akmal, M. Khan, L. Zhou, J. Lei, J. Zhang, A binary dumbbell visible light driven photocatalyst for simultaneous hydrogen production with the selective oxidation of benzyl alcohol to benzaldehyde, J. Colloid Interface Sci. 665 (2024) 911–921, https://doi.org/10.1016/j.jcis.2024.03.190.
[17] L. Huidobro, A. Domingo, E. Gómez, A. Serrà, Bismuth oxyiodide-based composites for advanced visible-light activation of peroxymonosulfate in pharmaceutical mineralization, Chemosphere 366 (2024) 143532, https://doi.org/10.1016/j.chemosphere.2024.143532.
[18] R. Bujaldón, M. Benamara, R. Dhahri, E. Gómez, A. Serrà, Attuning doped ZnO-based composites for an effective light-driven mineralization of pharmaceuticals via PMS activation, Chemosphere 357 (2024), https://doi.org/10.1016/j.chemosphere.2024.142127.
[19] C. Liu, S. Mao, H. Wang, Y. Wu, F. Wang, M. Xia, Q. Chen, Peroxymonosulfate-assisted for facilitating photocatalytic degradation performance of 2D/2D WO_3/BiOBr S-scheme heterojunction, Chem. Eng. J. 430 (2022) 132806, https://doi.org/10.1016/j.cej.2021.132806.
[20] W. Wang, F. Song, C. Du, Y. Su, Durable and eco-friendly peroxymonosulfate activation over cobalt/tin oxides-based heterostructures for antibiotics removal: insight to mechanism, degradation pathway, J. Colloid Interface Sci. 625 (2022) 479–492, https://doi.org/10.1016/j.jcis.2022.06.056.
[21] M. Tayyab, U.E. Kulsoom, Y. Liu, S. Mansoor, M. Khan, Z. Akmal, A. Mushtaq, M. Arif, U. Shamriaz, L. Zhou, J. Lei, J. Zhang, Visible light-driven photocatalytic H_2 evolution and dye degradation by electrostatic self-assembly of CdS nanowires on Nb_2C MXene, Int. J. Hydrog. Energy 51 (2023) 1400–1413, https://doi.org/10.1016/j.ijhydene.2023.09.199.
[22] L. Huidobro, Q. Bautista, M. Alinezhadfar, E. Gómez, A. Serrà, Enhanced visible-light-driven peroxymonosulfate activation for antibiotic mineralization using electrosynthesized nanostructured bismuth oxyiodides thin films, J. Environ. Chem. Eng. 12 (2024) 112545, https://doi.org/10.1016/j.jece.2024.112545.
[23] T. Tang, G. Lu, W. Wang, R. Wang, K. Huang, Z. Qiu, X. Tao, Z. Dang, Photocatalytic removal of organic phosphate esters by TiO_2: effect of inorganic ions and humic acid, Chemosphere 206 (2018) 26–32, https://doi.org/10.1016/j.chemosphere.2018.04.161.
[24] M. Hjiri, R. Bujaldón, J. Lloreda, E. Gómez, A. Serrà, Advanced degradation of organic pollutants using sonophotocatalytic peroxymonosulfate activation with $CoFe_2O_4$/Cu- and Ce-doped SnO_2 composites, Chemosphere 354 (2024) 141656, https://doi.org/10.1016/j.chemosphere.2024.141656.
[25] J.P. Randall, M.A.B. Meador, S.C. Jana, Tailoring mechanical properties of aerogels for aerospace applications, ACS Appl. Mater. Interfaces 3 (2011) 613–626, https://doi.org/10.1021/am200007n.
[26] J. Biener, M. Stadermann, M. Suss, M.A. Worsley, M.M. Biener, K.A. Rose, T. F. Baumann, Advanced carbon aerogels for energy applications, Energy Environ. Sci. 4 (2011) 656–667, https://doi.org/10.1039/c0ee00627k.
[27] M.A. Worsley, P.J. Pauzauskie, T.Y. Olson, J. Biener, J.H.J. Satcher, T.F. Baumann, Synthesis of graphene aerogel with high electrical conductivity, J. Am. Chem. Soc. 132 (2010) 14067–14069, https://doi.org/10.1021/ja1072299.
[28] T.-Y. Wei, C.-H. Chen, H.-C. Chien, S.-Y. Lu, C.-C. Hu, A cost-effective supercapacitor material of ultrahigh specific capacitances: spinel nickel cobaltite aerogels from an epoxide-driven Sol–Gel process, Adv. Mater. 22 (2010) 347–351, https://doi.org/10.1002/adma.200902175.
[29] J.-H. Kim, D.J. Suh, T.-J. Park, K.-L. Kim, Effect of metal particle size on coking during CO_2 reforming of CH_4 over Ni–alumina aerogel catalysts, Appl. Catal. A Gen. 197 (2000) 191–200, https://doi.org/10.1016/S0926-860X(99)00487-1.
[30] R. Al-Oweini, H. El-Rassy, Synthesis and characterization by FTIR spectroscopy of silica aerogels prepared using several $Si(OR)_4$ and $R''Si(OR')_3$ precursors, J. Mol. Struct. 919 (2009) 140–145, https://doi.org/10.1016/j.molstruc.2008.08.025.
[31] H. Maleki, Recent advances in aerogels for environmental remediation applications: a review, Chem. Eng. J. 300 (2016) 98–118, https://doi.org/10.1016/j.cej.2016.04.098.
[32] T. Pan, X. Cui, Gelatin aerogel with good mechanical properties and adjustable physical properties for boron adsorption from salt lake brines: an optimized process, Int. J. Biol. Macromol. 251 (2023) 126403, https://doi.org/10.1016/j.ijbiomac.2023.126403.
[33] F. Shi, C. Chen, J. Liu, T. Yu, X. Wang, Construction of activated-CNT/carbon composite aerogel for supercapacitor electrode with ultra high cycle stability, J. Solid State Chem. 330 (2024) 124492, https://doi.org/10.1016/j.jssc.2023.124492.
[34] M.A. Worsley, P.J. Pauzauskie, S.O. Kucheyev, J.M. Zaug, A.V. Hamza, J. H. Satcher, T.F. Baumann, Properties of single-walled carbon nanotube-based aerogels as a function of nanotube loading, Acta Mater. 57 (2009) 5131–5136, https://doi.org/10.1016/j.actamat.2009.07.012.
[35] W. Chen, X. Yang, J. Huang, Y. Zhu, Y. Zhou, Y. Yao, C. Li, Iron oxide containing graphene/carbon nanotube based carbon aerogel as an efficient E-Fenton cathode for the degradation of methyl blue, Electrochim. Acta 200 (2016) 75–83, https://doi.org/10.1016/j.electacta.2016.03.044.
[36] M.A. Worsley, J.H.J. Satcher, T.F. Baumann, Synthesis and characterization of monolithic carbon aerogel nanocomposites containing double-walled carbon nanotubes, Langmuir 24 (2008) 9763–9766, https://doi.org/10.1021/la8011684.
[37] C.V. Manzano, L. Philippe, A. Serrà, Recent progress in the electrochemical deposition of ZnO nanowires: synthesis approaches and applications, Crit. Rev. Solid State Mater. Sci. 47 (5) (2021) 772–805, https://doi.org/10.1080/10408436.2021.1989663.
[38] R. Atchudan, T.N.J.I. Edison, S. Perumal, M. Shanmugam, Y.R. Lee, Direct solvothermal synthesis of zinc oxide nanoparticle decorated graphene oxide nanocomposite for efficient photodegradation of azo-dyes, J. Photochem. Photobiol. A Chem. 337 (2017) 100–111, https://doi.org/10.1016/j.jphotochem.2017.01.021.
[39] J. Theerthagiri, S. Salla, R.A. Senthil, P. Nithyadharseni, A. Madankumar, P. Arunachalam, T. Maiyalagan, H.-S. Kim, A review on ZnO nanostructured materials: energy, environmental and biological applications, Nanotechnology 30 (2019) 392001, https://doi.org/10.1088/1361-6528/ab268a.
[40] A. Serrà, Y. Zhang, B. Sepúlveda, E. Gómez, J. Nogués, J. Michler, L. Philippe, Highly active ZnO-based biomimetic fern-like microleaves for photocatalytic water decontamination using sunlight, Appl. Catal. B Environ. 248 (2019) 129–146, https://doi.org/10.1016/j.apcatb.2019.02.017.
[41] W. Jia, Y. Shang, L. Gong, X. Chen, Synthesis of Al-ZnO nanocomposite and its potential application in photocatalysis and electrochemistry, Inorg. Chem. Commun. 88 (2018) 51–55, https://doi.org/10.1016/j.inoche.2017.12.013.
[42] R. Yousefi, F. Jamali-Sheini, M. Cheraghizade, S. Khosravi-Gandomani, A. Sáaedi, N.M. Huang, W.J. Basirun, M. Azarang, Enhanced visible-light photocatalytic activity of strontium-doped zinc oxide nanoparticles, Mater. Sci. Semicond. Process. 32 (2015) 152–159, https://doi.org/10.1016/j.mssp.2015.01.013.
[43] K.M. Lee, C.W. Lai, K.S. Ngai, J.C. Juan, Recent developments of zinc oxide based photocatalyst in water treatment technology: a review, Water Res. 88 (2016) 428–448, https://doi.org/10.1016/j.watres.2015.09.045.
[44] M. Qi, Q. Hou, S. Sha, M. Chen, First-principles of Be/Mg/Ca doping and point defects of VZn and Hi in the magnetic and optical properties of ZnO, Mater. Sci. Semicond. Process. 131 (2021) 105857, https://doi.org/10.1016/j.mssp.2021.105857.
[45] H. Zhai, L. Wang, D. Sun, D. Han, B. Qi, X. Li, L. Chang, J. Yang, Direct sunlight responsive Ag-ZnO heterostructure photocatalyst: enhanced degradation of rhodamine B, J. Phys. Chem. Solids 78 (2015) 35–40, https://doi.org/10.1016/j.jpcs.2014.11.004.
[46] M. Benamara, K.I. Nassar, M. Essid, S. Frick, R. Rugmini, K.C. Sekhar, J.P.B. Silva, Visible light-driven removal of rhodamine B using indium-doped zinc oxide prepared by Sol–Gel method, J. Sol-Gel Sci. Technol. 111 (2024) 553–565, https://doi.org/10.1007/s10971-024-06471-0.
[47] J. Kim, G.V. Naik, A.V. Gavrilenko, K. Dondapati, V.I. Gavrilenko, S.M. Prokes, O. J. Glembocki, V.M. Shalaev, A. Boltasseva, Optical properties of gallium-doped zinc oxide-a low-loss plasmonic material: first-principles theory and experiment, Phys. Rev. X 3 (2014) 1–9, https://doi.org/10.1103/PhysRevX.3.041037.
[48] M. Ahmad, E. Ahmed, Y. Zhang, N.R. Khalid, J. Xu, M. Ullah, Z. Hong, Preparation of highly efficient Al-doped ZnO photocatalyst by combustion synthesis, Curr. Appl. Phys. 13 (2013) 697–704, https://doi.org/10.1016/j.cap.2012.11.008.
[49] J. Zou, J. Liu, A.S. Karakoti, A. Kumar, D. Joung, Q. Li, S.I. Khondaker, S. Seal, L. Zhai, Ultralight multiwalled carbon nanotube aerogel, ACS Nano 4 (2010) 7293–7302, https://doi.org/10.1021/nn102246a.
[50] E.A. Mwafy, Eco-friendly approach for the synthesis of MWCNTs from waste tires via chemical vapor deposition, Environ. Nanotechnol. Monit. Manag. 14 (2020) 100342, https://doi.org/10.1016/j.enmm.2020.100342.
[51] M. Kakazey, M. Serrano, M. Vlasova, V.A. Basiuk, E.V. Basiuk, V. Gómez-Vidales, P. J. Sebastian, Evolution of morphology and defect states in mechanically processed ZnO+xMWCNTs nanosystems, J. Alloys Compd. 762 (2018) 605–615, https://doi.org/10.1016/j.jallcom.2018.05.176.
[52] M. Amir, H.A.L. Chaghouri, Y. Iqbal, S. Ali, M. Amin, Enhancement of CO gas sensing with ZnO nanostructures on MWCNTs films, Ceram. Int. 50 (2024) 48768–48778, https://doi.org/10.1016/j.ceramint.2024.09.230.
[53] M.R. Benzigar, S.N. Talapaneni, S. Joseph, K. Ramadass, G. Singh, J. Scaranto, U. Ravon, K. Al-Bahily, A. Vinu, Recent advances in functionalized micro and mesoporous carbon materials: synthesis and applications, Chem. Soc. Rev. 47 (2018) 2680–2721, https://doi.org/10.1039/c7cs00787f.
[54] B.J. Melde, B.J. Johnson, Mesoporous materials in sensing: morphology and functionality at the meso-interface, Anal. Bioanal. Chem. 398 (2010) 1565–1573, https://doi.org/10.1007/s00216-010-3688-6.
[55] Y. Song, F. Yin, C. Zhang, W. Guo, L. Han, Y. Yuan, Three-dimensional ordered mesoporous carbon spheres modified with ultrafine zinc oxide nanoparticles for enhanced microwave absorption properties, Nano-Micro Lett. 13 (2021) 76, https://doi.org/10.1007/s40820-021-00601-x.
[56] H. Peng, W. Xiong, Z. Yang, Z. Xu, J. Cao, M. Jia, Y. Xiang, Advanced MOFs@aerogel composites: construction and application towards environmental remediation, J. Hazard. Mater. 432 (2022) 128684, https://doi.org/10.1016/j.jhazmat.2022.128684.
[57] H. Maleki, N. Hüsing, Current status, opportunities and challenges in catalytic and photocatalytic applications of aerogels: environmental protection aspects, Appl. Catal. B Environ. 221 (2018) 530–555, https://doi.org/10.1016/j.apcatb.2017.08.012.
[58] R. Ganesamoorthy, V.K. Vadivel, R. Kumar, O.S. Kushwaha, H. Mamane, Aerogels for water treatment: a review, J. Clean. Prod. 329 (2021) 129713, https://doi.org/10.1016/j.jclepro.2021.129713.

[59] W. Liang, S.J. Couperthwaite, G. Kaur, C. Yan, D.W. Johnstone, G.J. Millar, Effect of strong acids on red mud structural and fluoride adsorption properties, J. Colloid Interface Sci. 423 (2014) 158–165, https://doi.org/10.1016/j.jcis.2014.02.019.
[60] S.A. Shah, H. Ali, M.I. Inayat, E.E. Mahmoud, H.A.L. Garalleh, B. Ahmad, Effect of carbon nanotubes and zinc oxide on electrical and mechanical properties of polyvinyl alcohol matrix composite by electrospinning method, Sci. Rep. 14 (2024) 1–13, https://doi.org/10.1038/s41598-024-79477-x.
[61] M. Khairy, M.M. Mohamed, A. Ibrahem, Enhanced the catalytic activity of reduction of 4-nitrophenol on Ag/RGO nanocomposites, J. Basic Environ. Sci. 5 (2024) 101–114, https://doi.org/10.21608/jbes.2024.370421.
[62] G.R. Dillip, A.N. Banerjee, V.C. Anitha, B. Deva Prasad Raju, S.W. Joo, B.K. Min, Oxygen vacancy-induced structural, optical, and enhanced supercapacitive performance of zinc oxide anchored graphitic carbon nanofiber hybrid electrodes, ACS Appl. Mater. Interfaces 8 (2016) 5025–5039, https://doi.org/10.1021/acsami.5b12322.
[63] F. Anjum, A.M. Asiri, M.A. Khan, M.I. Khan, S.B. Khan, K. Akhtar, E.M. Bakhsh, K. A. Alamry, S.Y. Alfifi, S. Chakraborty, Photo-degradation, thermodynamic and kinetic study of carcinogenic dyes via zinc oxide/graphene oxide nanocomposites, J. Mater. Res. Technol. 15 (2021) 3171–3191, https://doi.org/10.1016/j.jmrt.2021.09.086.
[64] G. Yashni, A.A. Al-Gheethi, R.M.S.R. Mohamed, M.K. Amir Hashim, Green synthesis of ZnO nanoparticles by *Coriandrum sativum* leaf extract: structural and optical properties, Desalin, Desalin. Water Treat. 167 (2019) 245–257, https://doi.org/10.5004/dwt.2019.24584.
[65] M. Yousuf, A. Mollah, T.R. Hess, Y.-N. Tsai, D.L. Cocke, An FTIR and XPS investigations of the effects of carbonation on the solidification/stabilization of cement based systems-Portland type V with zinc, Cem. Concr. Res. 23 (1993) 773–784, https://doi.org/10.1016/0008-8846(93)90031-4.
[66] J. Nomoto, H. Makino, T. Tsuchiya, T. Yamamoto, Chemical trends of n -type doping of Al, Ga, In, and Ti donors for ZnO polycrystalline films deposited by direct-current magnetron sputtering, J. Appl. Phys. 128 (2020) 145303, https://doi.org/10.1063/5.0021613.
[67] B. Abebe, N.K. Gupta, D. Tsegaye, A critical mini-review on doping and heterojunction formation in ZnO-based catalysts, RSC Adv. 14 (2024) 17338–17349, https://doi.org/10.1039/d4ra02568g.
[68] S. Boscarino, S. Filice, A. Sciuto, S. Libertino, M. Scuderi, C. Galati, S. Scalese, Investigation of ZnO-decorated CNTs for UV light detection applications, Nanomaterials 9 (2019) 1–12, https://doi.org/10.3390/nano9081099.
[69] A.U. Rehman, M. Atif, S. Baqi, A. Ul-Hamid, U. ur Rehman, W. Khalid, Z. Ali, F.C.-C. Ling, M. Nadeem, Enhancement in the electromagnetic shielding properties of doped $M_{0.01}Fe_{2.99}O_4$ magnetite nanoparticles (M=Mn^{2+},Ni^{2+},Cu^{2+},Zn^{2+}), J. Alloys Compd. 960 (2023) 171051, https://doi.org/10.1016/j.jallcom.2023.171051.
[70] M. Benamara, A. Ly, S. Soltani, M. Essid, H. Dahman, R. Dhahri, L. El Mir, M. Debliquy, D. Lahem, Enhanced detection of low concentration volatile organic compounds using advanced doped zinc oxide sensors, RSC Adv. 13 (2023) 30230–30242, https://doi.org/10.1039/d3ra03143h.
[71] M. Benamara, P. Rivero-Antúnez, H. Dahman, M. Essid, S. Bouzidi, M. Debliquy, D. Lahem, V. Morales-Flórez, L. Esquivias, J.P.B. Silva, L. El Mir, Selective and rapid detection of acetone using aluminum-doped zno-based sensors, J. Sol-Gel Sci. Technol. 108 (2023) 13–27, https://doi.org/10.1007/s10971-023-06197-5.
[72] R. Dhahri, M. Hjiri, L.E. Mir, A. Bonavita, D. Iannazzo, S.G. Leonardi, G. Neri, CO sensing properties under UV radiation of Ga-doped ZnO nanopowders, Appl. Surf. Sci. 355 (2015) 1321–1326, https://doi.org/10.1016/j.apsusc.2015.08.198.
[73] D.H. Choi, S.M. Lee, D.W. Jeong, J.O. Lee, D.H. Ha, M.H. Bae, J.J. Kim, Tunneling spectroscopy for electronic bands in multi-walled carbon nanotubes with van der waals gap, Molecules 26 (2021) 1–10, https://doi.org/10.3390/molecules26082128.
[74] S. Landi, I.R. Segundo, E. Freitas, M. Vasilevskiy, J. Carneiro, C.J. Tavares, Use and misuse of the Kubelka-Munk function to obtain the band gap energy from diffuse reflectance measurements, Solid State Commun. 341 (2022) 114573, https://doi.org/10.1016/j.ssc.2021.114573.
[75] N. Sangiorgi, L. Aversa, R. Tatti, R. Verucchi, A. Sanson, Spectrophotometric method for optical band gap and electronic transitions determination of semiconductor materials, Opt. Mater. (Amst). 64 (2017) 18–25, https://doi.org/10.1016/j.optmat.2016.11.014.
[76] T. Zhang, M. Li, J. Chen, Y. Wang, L. Miao, Y. Lu, Y. He, Multi-component ZnO alloys: bandgap engineering, hetero-structures, and optoelectronic devices, Mater. Sci. Eng. R. Rep. 147 (2022) 100661, https://doi.org/10.1016/j.mser.2021.100661.
[77] Z. Bahri, B. Rezai, E. Kowsari, Selective separation of gallium from zinc using flotation: effect of solution pH value and the separation mechanism, Miner. Eng. 86 (2016) 104–113, https://doi.org/10.1016/j.mineng.2015.12.005.
[78] M. Younas, M.A. Gondal, M.A. Dastageer, K. Harrabi, Efficient and cost-effective dye-sensitized solar cells using MWCNT-TiO2 nanocomposite as photoanode and MWCNT as Pt-free counter electrode, Sol. Energy 188 (2019) 1178–1188, https://doi.org/10.1016/j.solener.2019.07.009.
[79] H. Yang, Z. Ding, Y. Liu, S. Zhang, Y. Zou, G. Bai, Y. Zhang, S. Xia, Biomass-derived carbon aerogel for peroxymonosulfate activation to remove tetracycline: carbonization temperature, oxygen-containing functional group content, and defect degree, Ind. Crop. Prod. 177 (2022) 114437, https://doi.org/10.1016/j.indcrop.2021.114437.
[80] D. Saravanakkumar, H.A. Oualid, Y. Brahmi, A. Ayeshamariam, M. Karunanaithy, A.M. Saleem, K. Kaviyarasu, S. Sivaranjani, M. Jayachandran, Synthesis and characterization of CuO/ZnO/CNTs thin films on copper substrate and its photocatalytic applications, OpenNano 4 (2019) 100025, https://doi.org/10.1016/j.onano.2018.11.001.
[81] J. Liu, Y. Dong, Q. Liu, W. Liu, H. Lin, MoS_2-based nanocomposites and aerogels for antibiotic pollutants removal from wastewater by photocatalytic degradation process: a review, Chemosphere 354 (2024) 141582, https://doi.org/10.1016/j.chemosphere.2024.141582.
[82] Y. Wu, W. Ren, Y. Li, J. Gao, X. Yang, J. Yao, Zeolitic Imidazolate Framework-67@Cellulose aerogel for rapid and efficient degradation of organic pollutants, J. Solid State Chem. 291 (2020) 121621, https://doi.org/10.1016/j.jssc.2020.121621.
[83] Y. Wu, Y. Li, T. Zhao, X. Wang, V.I. Isaeva, L.M. Kustov, J. Yao, J. Gao, Bimetal-organic framework-derived Nanotube@Cellulose aerogels for peroxymonosulfate (PMS) activation, Carbohydr. Polym. 296 (2022) 119969, https://doi.org/10.1016/j.carbpol.2022.119969.
[84] B. Cha, Y. Yea, K. Yun, T. Kim, H. Kim, Y. Yoon, S. Kim, C.M. Park, Enhanced catalytic oxidation of naproxen via activation of peroxymonosulfate by Fe-based metal–organic framework aerogels functionalized with Ag nanoparticles, J. Hazard. Mater. 458 (2023) 131847, https://doi.org/10.1016/j.jhazmat.2023.131847.
[85] W. Ren, J. Gao, C. Lei, Y. Xie, Y. Cai, Q. Ni, J. Yao, Recyclable metal-organic framework/cellulose aerogels for activating peroxymonosulfate to degrade organic pollutants, Chem. Eng. J. 349 (2018) 766–774, https://doi.org/10.1016/j.cej.2018.05.143.